Journal of Asian Earth Sciences 113 (2015) 454–470

Contents lists available at ScienceDirect

Journal of Asian Earth Sciences

journal homepage: www.elsevier.com/locate/jseaes

Geochronology, geochemistry and geodynamic implications of the Late Mesozoic volcanic rocks in the southern Great Xing'an Mountains, NE China

Wu-Bin Yang [a,b], He-Cai Niu [a,b,*], Li-Ren Cheng [c], Qiang Shan [a], Ning-Bo Li [a,d]

[a] Key Laboratory of Mineralogy and Metallogeny, Guangzhou Institute of Geochemistry, Chinese Academy of Sciences, Guangzhou 510640, China
[b] Guangdong Provincial Key Laboratory of Mineral Physics and Materials, Guangzhou 510640, China
[c] College of Earth Science, Jilin University, Changchun 130061, China
[d] Graduate University of Chinese Academy of Sciences, Beijing 100049, China

ARTICLE INFO

Article history:
Received 20 June 2014
Received in revised form 21 November 2014
Accepted 4 December 2014
Available online 6 January 2015

Keywords:
Mesozoic igneous event
Calc-alkaline and shoshonitic rocks
Subduction-modified lithospheric mantle
Central Asian Orogenic Belt (CAOB)
NE China

ABSTRACT

Large-scale Mesozoic volcanisms in the Great Xing'an Mountains (GXM), northeastern (NE) China, are being extensively interested recently. However, the petrogenesis and geodynamic implications of these volcanic rocks are still on controversy. In this study, geochronology and geochemistry of the intermediate and felsic volcanic rocks of Late Mesozoic from the southern GXM was investigated. Zircon U–Pb geochronology yields $^{206}Pb/^{238}U$ ages ranging from 154.3 ± 1.7 Ma to 127.0 ± 2.4 Ma for the eight selected volcanic rocks, where the major period of the Mesozoic volcanisms is constrained during the Early Cretaceous. The presented volcanic rocks are andesite–trachydacite–rhyolite and show calc-alkaline to shoshonitic features. They have elevated incompatible trace element concentrations and significantly negative Nb–Ta–Ti and positive Pb anomalies, which display characteristics of typical subduction-related magmas rather than within-plate magmatic signature. Sr–Nd isotopic data indicate that their magma sources were mixed with proportions of old crustal components. Geochemical features, therefore, indicate that the intermediate and felsic shoshonitic magma was plausibly derived from partial melting of the subduction-modified lithospheric mantle and thickened lower crust, respectively, induced by delamination and/or asthenosphere upwelling in extensional setting. Combined with the tectonic evolution of the Great Xing'an area, we propose a hypothesis that the large-scale Mesozoic volcanisms in NE China were controlled by the transition of regional stress from southward to westward, which are induced by the changes of tectonic regimes from the previous Mongol–Okhotsk subduction to the succeeding paleo-Pacific subduction during Late Mesozoic.

1. Introduction

Mesozoic volcanisms are widespread throughout northeastern China and its adjacent areas (Fig. 1a). In the Great Xing'an area, the Mesozoic volcanic rocks cover an area of ca. 100,000 km^2 (Ying et al., 2010), and mainly distribute along the GXM. Numerous geological, petrological and geochronological studies were carried out on these large-scale magmatic activities (Jahn et al., 2001; Fan et al., 2003; Wu et al., 2005; Wang et al., 2006; Zhang et al., 2008a, 2008b, 2010; Guo et al., 2010; Yang et al., 2013), which have not resulted in a consensus about the mechanism. There are several models has been proposed to interpret this extensive Mesozoic magmatism, including: mantle plume hypothesis (Lin et al., 1998; Ge et al., 1999), post-orogenic diffuse extension after the subduction of the Mongol–Okhotsk Ocean (Fan et al., 2003; Gao et al., 2005; Guo et al., 2010), thickened lithospheric delaminating induced by the subduction of Pacific plate (Wu et al., 2005; Wang et al., 2006; Zhang et al., 2010).

It has been proposed that partial melting of subducted sediments could modify the nature of the subcontinental lithospheric mantle (SCLM) and produce vein networks of clinopyroxene/amphibole/phlogopite minerals within the mantle wedge (Pilet et al., 2008; Hermann and Rubatto, 2009; Skora and Blundy, 2010; Yang et al., 2014a). Partial melting of those pure vein minerals will generate ultrapotassic magmas, whereas increasing interaction between these veins and the surrounding mantle will decrease the alkaline component and result in relatively low-K

* Corresponding author at: Key Laboratory of Mineralogy and Metallogeny, Guangzhou Institute of Geochemistry, Chinese Academy of Sciences, Guangzhou 510640, China.
E-mail address: niuhc@gig.ac.cn (H.-C. Niu).

http://dx.doi.org/10.1016/j.jseaes.2014.12.002
1367-9120/

shoshonitic and calc-alkaline rocks (Avanzinelli et al., 2009; Conticelli et al., 2009a, 2009b). This genetic model has been applied to shoshonitic series rocks associated with ultrapotassic rocks, high-K calc-alkaline rocks, or even to calc-alkaline rocks (e.g., Duggen et al., 2005; Altherr et al., 2008; Avanzinelli et al., 2009; Conticelli et al., 2009a; Yang et al., 2012). On the other hand,

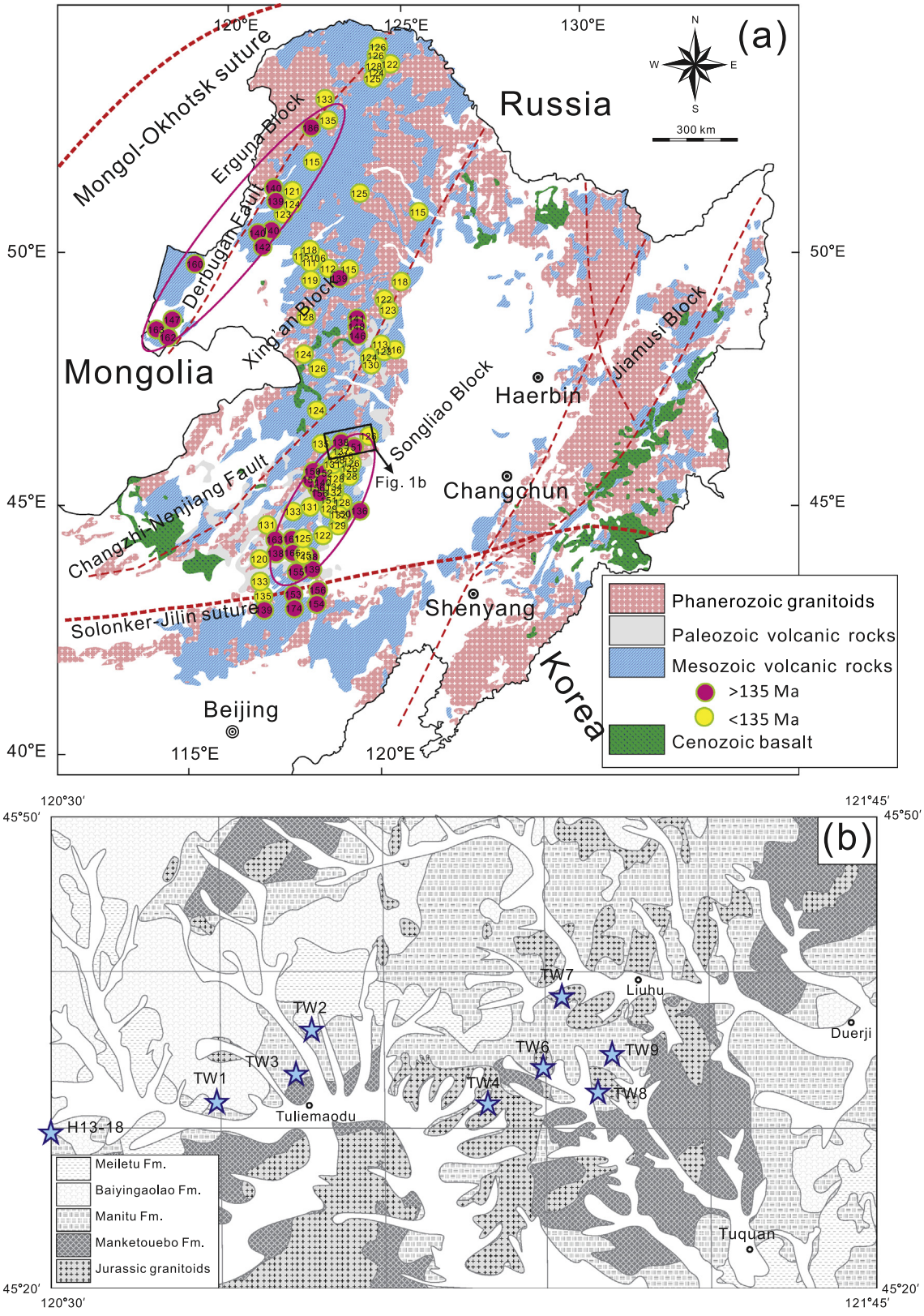

Fig. 1. (a) Simplified tectonic units of northeastern China showing the distribution of the Mesozoic volcanic rocks (after Guo et al. (2010)). The marked ages of Late Mesozoic volcanic rocks in the GXM are referenced from Wang et al. (2006), Zhang et al. (2008a,b, 2010), Ying et al. (2010) and Li et al. (2013). (b) Geological map and sample locations of the study area in the southern GXM.

K-rich shoshonitic magma also can be derived from partial melting of the thickened lower crust, following underplating by mantle-derived magma in a post-collisional extension setting (Kuster and Harms, 1998; Jiang et al., 2002; Campbell et al., 2014; Liu et al., 2014).

In NE China, the GXM corresponds to not only a sharp gravity anomaly and east–west topographic boundary, but also a boundary that penetrates the lithosphere (Zhang et al., 2010 and references therein). The widespread volcanic rocks in the southern GXM are mainly sub-alkaline and show characteristics of calc-alkaline and shoshonitic series. Recent geochronological studies indicate the volcanic rocks in the Great Xing'an area were mainly erupted in the Early Cretaceous (Wu et al., 2005; Wang et al., 2006; Zhang et al., 2010). In this study, we systematically investigate a suite of calc-alkaline and shoshonitic volcanic rocks from the southern GXM on geochronology and geochemistry. The results include high quality zircon U–Pb age data, whole rock major and trace element compositions, and Sr–Nd isotopes. These data allow us to reveals the petrogenesis of the Mesozoic volcanic rocks and its geodynamic setting. Combined with previously published data from the adjacent regions, the geochemical and geochronological data are then to evaluate the evolution of magmatism in the GXM, and further NE China.

2. Geological background

The Central Asian Orogenic Belt (CAOB) is an accretionary orogen that stretches from the Ural Mountains to the Pacific Ocean (Jahn, 2004). The eastern part of the CAOB is termed as the Xingmeng (Xing'an–Mongolian) orogenic belt in the Chinese literature. The Xingmeng orogenic belt represents a collage of four microcontinental blocks, in which the Songliao, Xing'an and Erguna blocks were amalgamated in Paleozoic, and the Jiamusi block docked to the east of Songliao block in Mesozoic (Wu et al., 2002, 2011). The Xing'an block comprises the Great Xing'an Range and Halar Basin. The Xing'an Block is mostly located in the GXM and is characterized by voluminous Mesozoic granite and volcanic rocks (Wu et al., 2000, 2011; Jahn et al., 2001; Wang et al., 2006; Guo et al., 2010; Yang et al., 2014b).

The southern segment of the GXM, which extends into Heilongjiang and Jilin Provinces in the east and the Inner Mongolia in the west, was the focus of this study. The volcanic rocks in the southern GXM are mainly distributed in several discrete basins, including the Baoshi, Pingshan and Wudan basins, and have been subdivided into the Manketouebo, Manitu, Baiyingaolao and Meiletu formations (Fig. 2; IMBGMR, 1991; Ying et al., 2010; Zhang et al., 2010). The Manketouebo formation is widely distributed and mainly composed of rhyolite, dacite, volcaniclastic rock and rhyolitic tuff. This basal formation unconformably overlie with the sedimentary rocks of the Jurassic Xinmin/Wanbao formation. The dacite is porphyritic with quartz, sanidine and plagioclase as phenocrysts. The matrix is mainly composed of volcanic glass. The Manitu formation is usually exposed along with the Manketouebo formation, but is less extensive than the latter. This formation mainly consists of andesite, trachydacite and volcaniclastic rocks, and conformably underlain by the Manketouebo formation. The andesite and trachydacite are porphyritic and hyalopilitic. The phenocrysts include plagioclase, amphibole, biotite and minor pyroxene. The matrix is composed of andesine and volcanic glass. Amygdaloidal structure sometimes occurred in the andesite, with the calcite and agate filling amygdules. The Baiyingaolao formation is distributed far less extensive than the Manketouebo and Manitu formations. It is characterized with the intercalated volcanic rocks and sedimentary rocks. The volcanic rocks consist of trachyte, rhyolite and rhyolitic volcaniclastic rocks, while the sedimentary rocks

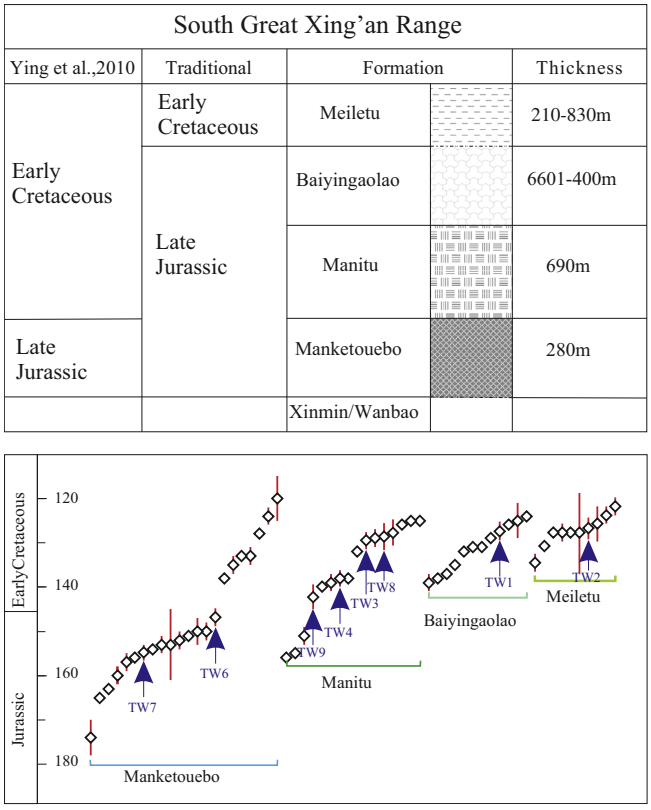

Fig. 2. Stratigraphic subdivision and age distribution of the Mesozoic volcanic strata in the southern GXM. Data are referred from Ying et al. (2010), Zhang et al. (2010), Li et al. (2013) and this study.

include tuffaceous sandstone, siltstone and shale. It conformably overlies the Manitu formation and in turns unconformably overlain by the Meiletu formation. The rhyolite has numerous felsophyric textures that are composed of crystalline quartz, K-feldspar, and minor plagioclase. The matrix is composed of andesine and volcanic glass. The Meiletu formation is composed of basalt, basaltic andesite, andesite, trachyte and intercalated volcaniclastic rocks. The andesite is usually porphyritic with plagioclase, amphibole and minor pyroxene as phenocrysts. The matrix is volcanic glass.

3. Analytical methods

3.1. Zircon U–Pb dating

Zircons were separated from the volcanic rocks using standard density and magnetic separation techniques and hand-picked under binocular microscope. Representative zircon grains were casted in an epoxy mount, and then were polished to near half sections to expose the internal structure for analysis. Polished zircons in epoxy mount were documented with transmitted and reflected light micrographs as well as cathodoluminescence (CL) images to reveal their internal textures (Fig. 3).

Zircon U–Pb dating of the volcanic rocks was undertaking by using an Agilent 7500a ICP-MS coupled with a Resonetics RESOlution M-50 193 nm laser-ablation system (LA-ICPMS) at the Key Laboratory of Isotope Geochronology and Geochemistry at the Guangzhou Institute of Geochemistry, Chinese Academy of Sciences (GIGCAS). Details on operating conditions for the laser ablation system and the ICP-MS instrument and data processing are described by Tu et al. (2011). All analyses were carried out at energy of 80 mJ, with a beam diameter of 31 μm and a repetition

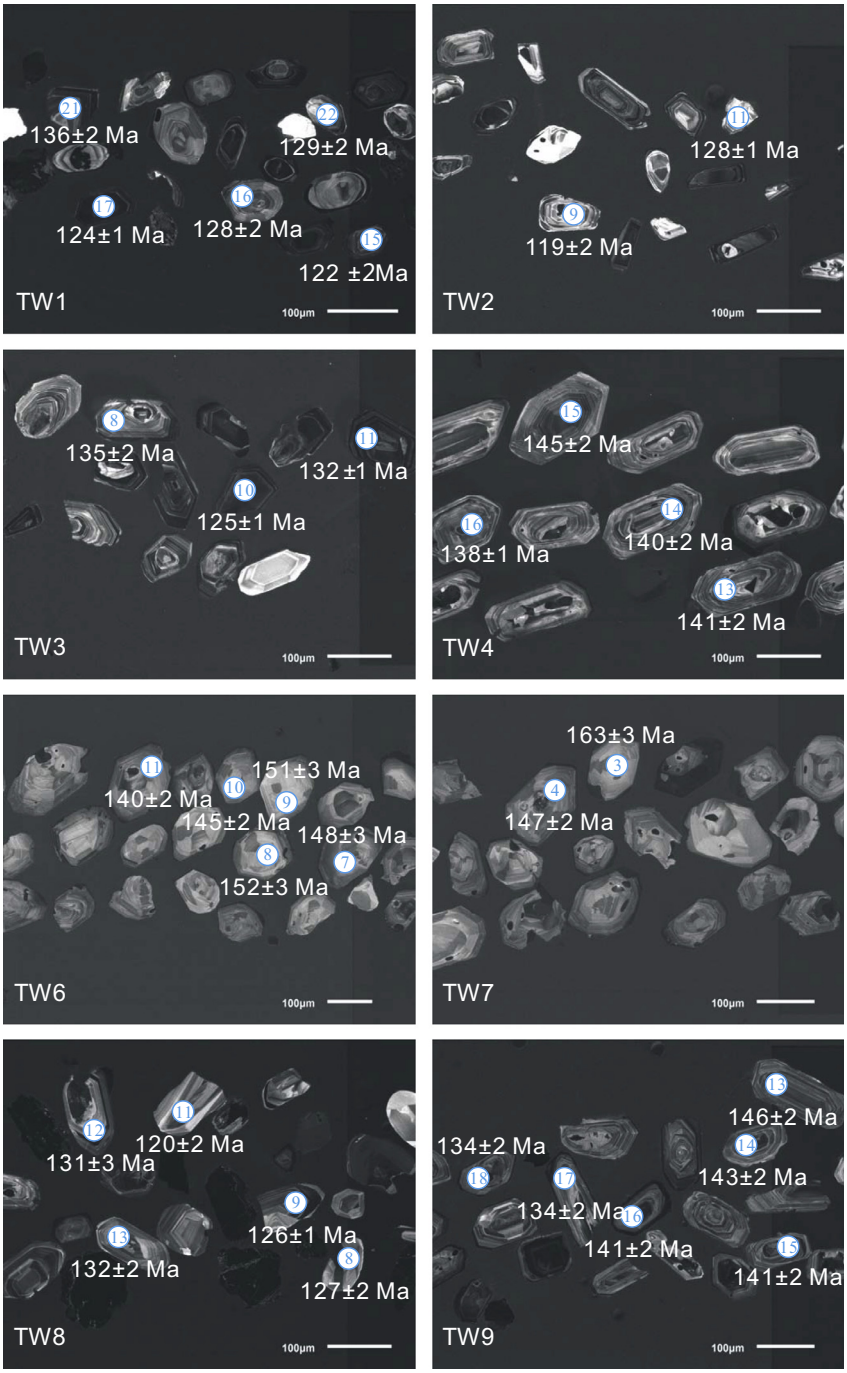

Fig. 3. Cathodoluminescence (CL) images of the presented eight volcanic samples from the southern GXM.

Table 1
Sample locations of the presented volcanic rocks in the southern GXM.

	Location	Latitude and longitude	Formation	Rock type	Age (Ma)	Period
TW2	Tuliemaodu	45°37′41″N; 120°54′06″E	Meiletu	Andesite	127.0 ± 2.4	Early Cretaceous
TW1	Tuliemaodu	45°31′10″N; 120°44′11″E	Baiyingaolao	Rhyolite	127.4 ± 2.1	
H13-18	Bayangeer	45°27′48″N; 120°28′25″E	Baiyingaolao	Rhyolite	–	
TW8	Tuquan	45°35′19″N; 121°20′38″E	Manitu	Andesite	127.7 ± 2.9	
TW3	Tuliemaodu	45°35′17″N; 120°55′23″E	Manitu	Andesite	129.5 ± 1.9	
TW4	Tuquan	45°32′19″N; 121°10′57″E	Manitu	Trachydacite	138.1 ± 1.9	
TW9	Tuquan	45°37′57″N; 121°22′54″E	Manitu	Trachydacite	142.2 ± 2.8	
TW6	Tuquan	45°35′45″N; 121°15′10″E	Manketouebo	Dacite	146.8 ± 2.0	Late Jurassic
TW7	Tuquan	45°38′42″N; 121°15′30″E	Manketouebo	Dacite	154.3 ± 1.7	

rate of 10 Hz. Helium was used as a carrier gas to enhance the transportation efficiency of the ablated material. TEM (417 Ma) was used as zircon standard (Black et al., 2003). An integration of background and analytical signals, and time-drift correction and quantitative calibration for trace element were undertaken by using the GLITTER 4.0 algorithm. The analytical data were reduced,

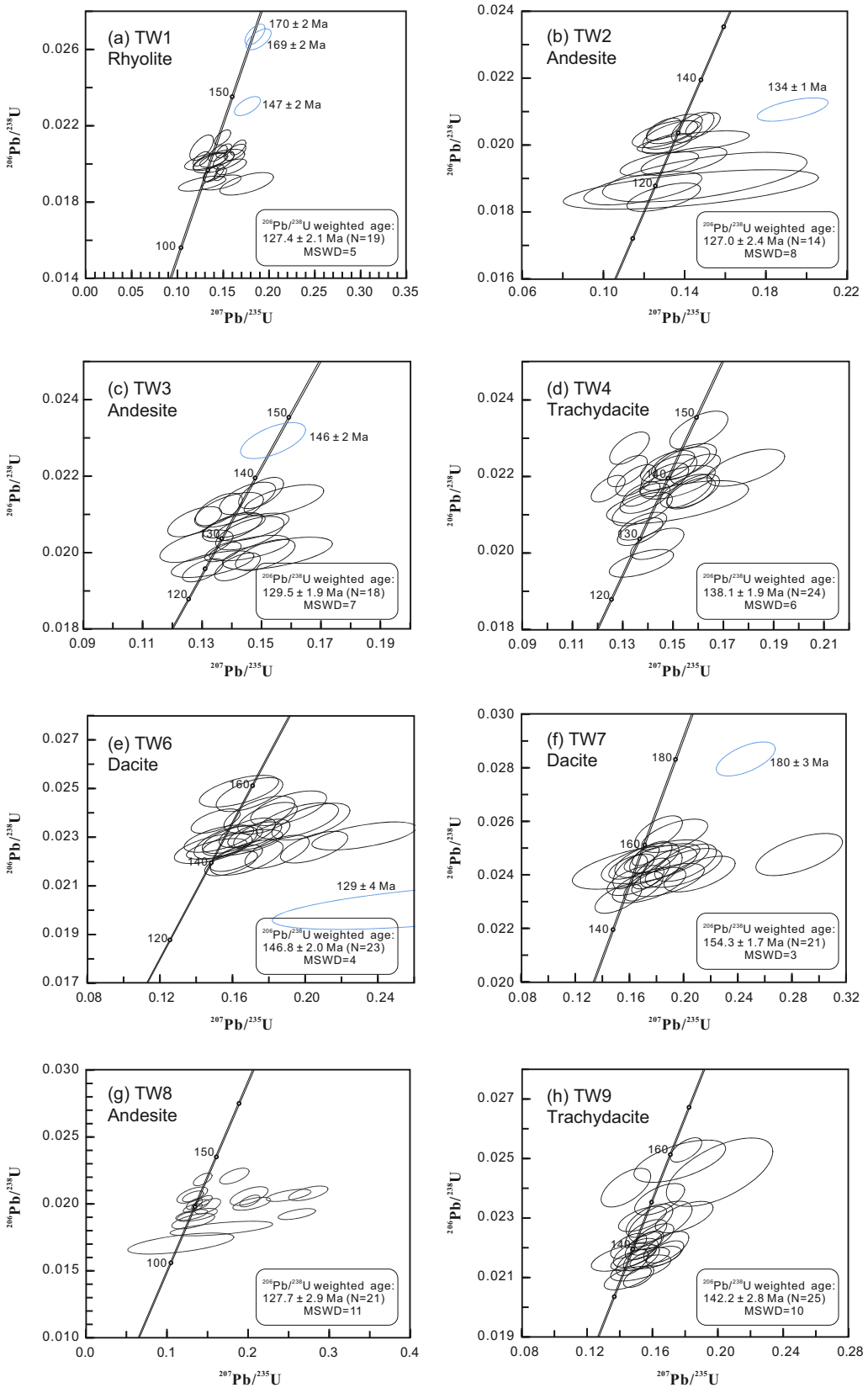

Fig. 4. Zircon LA-ICPMS U–Pb concordia diagrams of the eight selected volcanic rocks from the southern GXM. The zircon xenocrysts and disconcordia data, that are marked blue ellipses, are excluded in the age calculation.

calculated and plotted by using the Isoplot 3.0 programs of Ludwig (2003). Individual analysis in the Table 1 and the concordia diagram (Fig. 4) are presented with 1σ error and uncertainties in weighted mean ages are quoted at 2σ (95% confidence level).

3.2. Whole-rock geochemistry analyses

Both chemical and isotopic compositions were analyzed at GIGCAS. Unaltered or least-altered samples were selected by optical microscopy for geochemical analysis. The selected samples were powdered to less than 200 mesh by using an agate mortar for whole-rock trace elements and isotopes analyses. Major element oxides were determined using the X-ray fluorescence method of Li et al. (2005). Loss-on-ignition was obtained by determining the weight loss of samples ignited in a furnace at 900 °C for 2 h and allowed to cool in a desiccator to minimize moisture absorption, which can be a major source of error in carbonate LOI determination. Approximately 50 mg of powdered whole-rock sample was dissolved in high-pressure Teflon bombs with a mixture of HF + HNO_3. Trace elements were analyzed by inductively coupled plasma mass spectrometry, using a Perkin–Elmer Sciex ELAN 6000 instrument following the analytical procedures described by Liu et al. (1996). Rhodium was used as an internal standard to monitor signal drift during counting. Analytical precision for most elements is better than 3%.

For Sr–Nd isotope determination, sample powders were firstly dissolved in Teflon capsules with HF + HNO_3 acid. Strontium and REE were separated using cation columns, and then the Nd fractions were further separated using HDEHP-coated Kef columns. Isotopic measurement was performed on the Micromass Isoprobe multicollector mass spectrometer at GIGCAS, following analytical procedures described by Wei et al. (2002) and Liang et al. (2003). Measured $^{87}Sr/^{86}Sr$ and $^{143}Nd/^{144}Nd$ ratios were normalized to $^{86}Sr/^{88}Sr = 0.1194$ and $^{146}Nd/^{144}Nd = 0.7219$, respectively. The reported $^{87}Sr/^{86}Sr$ and $^{143}Nd/^{144}Nd$ ratios were respectively adjusted to the NBS SRM 987 standard with an $^{87}Sr/^{86}Sr$ value of 0.71025 and the Shin Etsu JNdi-1 standard with a $^{143}Nd/^{144}Nd$ value of 0.512115.

4. Results

4.1. Zircon U–Pb geochronology

The widespread Mesozoic volcanic rocks in the GXM were documented by numerous previous works (e.g., Wang et al., 2006; Zhang et al., 2008a, 2010; Ying et al., 2010; Wu et al., 2011). In the southern GXM, the large-scale volcanisms in the Late Mesozoic were re-evaluated based on the systematic and high precision isotopic ages (Ying et al., 2010; Zhang et al., 2010). Given that, we need to give a brief summary of the age distributions in this contribution for the Mesozoic volcanic strata in the southern GXM region, as shown in Fig. 2. All zircon crystals from the Mesozoic volcanic rocks of this study are transparent, light olive brown and prismatic. They are typical magmatic zircons with clear oscillatory zoning in their CL images (Fig. 3) and high Th/U ratios. The zircon U–Pb analyzing results are listed in Table 2 and related illustrations are shown in Fig. 4.

The Manketouebo formation is the lowest unit of the Mesozoic volcanic rocks in the southern GXM. Ages of this formation are ranging from 174 Ma to 120 Ma, as shown in Fig. 2. The age of 174 ± 4 Ma for a rhyolite 05FW060 (Zhang et al., 2010) of the Manketouebo formation is the oldest age so far reported, indicating the onset of Mesozoic volcanism in the southern GXM. Zircon grains extracted from two dacite TW6 and TW 7 are euhedral with oscillatory zonation, suggesting their magmatic origin. Twenty-one analyses of zircon from dacite TW7 define a weighted $^{206}Pb/^{238}U$ age of 154.3 ± 1.7 Ma (MSWD = 3), while one zircon grain has a much older age of 180 Ma. We interpret the former younger age as the crystallization age of the volcanic rock, and zircon grain with older age as zircon xenocryst. Twenty-three zircon grains from dacite TW6 yield a concordant age of 146.8 ± 2.0 Ma (MSWD = 4), without one grains of disconcordia age of 129 Ma.

Volcanic rocks of the Manitu formation have ages ranging from 125 Ma to 156 Ma (Fig. 2). Four volcanic rock samples were collected from this formation for zircon in situ U–Pb dating. Zircons from samples TW9, TW4, TW3 and TW8 are euhedral with prismatic morphology. Twenty-five analyses of zircons from trachyte TW9 yield a weighted $^{206}Pb/^{238}U$ age of 142.2 ± 2.8 Ma (MSWD = 10). Twenty-four zircon grains from trachyte TW4 yield a weighted mean age of 138.1 ± 1.9 Ma (MSWD = 6). Eighteen zircon grains from andesite TW3 define a weighted mean age of 129.5 ± 1.9 Ma (MSWD = 7), while one zircon xenocryst has a much older age of 146 Ma. Twenty-one analyses of zircon from andesite TW8 yield a weighted mean age of 127.7 ± 2.9 Ma (MSWD = 11). The four weighted mean ages of the volcanic rocks were regard to represent the crystallization ages of the four presented rocks.

Ages of the Baiyingaolao formation are ranging from 124 Ma to 139 Ma (Fig. 2). One rhyolite sample TW1 was collected from this formation, in which zircon grains are euhedral with apparent oscillatory zonation. Nineteen zircon grains yield a weighted mean age of 127.4 ± 2.1 Ma (MSWD = 5), while three zircon xenocrysts have clearly older ages of 147 Ma, 169 Ma and 170 Ma.

The Meiletu formation is the uppermost unit of the Mesozoic volcanic sequences in the southern GXM, and the volcanic activity terminated after the eruption of igneous rocks of this formation. Zircons from one andesite sample TW2 are euhedral with oscillatory zonation. Fourteen zircon grains yield a weighted mean age of 127.0 ± 2.4 Ma (MSWD = 8), without one grain of disconcordia age of 134 Ma.

4.2. Geochemistry of the Mesozoic volcanic rocks

The major and trace element chemistry for 15 representative samples of the Mesozoic volcanic rocks are presented in Table 3, in which nine samples are intermediate and the other six rhyolite samples are felsic. The intermediate volcanic rocks have intermediate SiO_2 contents (57.3–64.4 wt.%) and high Al_2O_3 (16.2–17.2 wt.%). They have K_2O contents ranging from 1.30 wt.% to 3.81 wt.%, MgO contents ranging from 1.24 wt.% to 3.27 wt.% and K_2O/Na_2O ratios from 0.29 to 1.01, consistent with the volcanic rocks being calc-alkaline to shoshonitic based on the criteria of Peccerillo and Taylor (1976). On the $Na_2O + K_2O$ versus SiO_2 classification diagram of Lebas et al. (1986), the intermediate volcanic rocks almost lie within the andesite–trachydacite fields (Fig. 5a). A plot of K_2O versus SiO_2 shows that most of the intermediate volcanic rocks in the southern GXM belong to the calc-alkaline–shoshonitic magma series (Fig. 5b).

The felsic volcanic rocks have high SiO_2 contents (68.9–70.4 wt.%) and high K_2O contents (5.17–6.32 wt.%). They have high contents of total alkalis, with $Na_2O + K_2O$ ranging from 9.33 wt.% to 10.2 wt.%, belong to alkaline rhyolite (Fig. 5a). They have MgO contents ranging from 0.36 wt.% to 0.46 wt.% and K_2O/Na_2O ratios from 1.25 to 1.69, consistent with the volcanic rocks being K-rich shoshonitic rocks (Fig. 5b). Both intermediate and felsic volcanic rocks have relatively low Mg-numbers, with values ranging from 38 to 52 and from 20 to 28, respectively (Table 3). LOI values of the volcanic rocks usually reflect the presence of hydrous mineral phases (e.g., amphiboles), carbonates and/or secondary minerals (e.g., chlorites). The elevated LOI values of 0.68–2.77 wt.% for both intermediate and felsic volcanic rocks show no correlation with La/Sm ratios, suggesting that alteration did not create significant

Table 2
Zircon LA-ICPMS U–Pb results of the eight selected volcanic rocks in the southern GXM.

Spots	Th (ppm)	U (ppm)	Th/U	Isotopic ratios ± 1σ						Ages ± 1σ (Ma)					
				$^{207}Pb/^{206}Pb$		$^{207}Pb/^{235}U$		$^{206}Pb/^{238}U$		$^{207}Pb/^{206}Pb$		$^{207}Pb/^{235}U$		$^{206}Pb/^{238}U$	
Rhyolite sample TW1															
TW1-01	570	1406	0.41	0.04362	0.00215	0.12647	0.00853	0.02086	0.00044	−90	104	121	8	133	3
TW1-02	576	1011	0.57	0.05234	0.00580	0.14545	0.01854	0.02016	0.00041	300	237	138	16	129	3
TW1-03	1568	2953	0.53	0.05676	0.00205	0.16305	0.00779	0.02062	0.00028	482	78	153	7	132	2
TW1-04	2228	3489	0.64	0.05139	0.00396	0.14335	0.01251	0.02023	0.00026	258	170	136	11	129	2
TW1-05	1206	3191	0.38	0.05231	0.00144	0.15073	0.00564	0.02070	0.00024	299	61	143	5	132	2
TW1-06	1373	1962	0.70	0.04546	0.00163	0.12609	0.00587	0.02028	0.00025	−31	70	121	5	129	2
TW1-07	730	1314	0.56	0.05454	0.00201	0.15044	0.00754	0.02021	0.00031	393	81	142	7	129	2
TW1-08	623	1089	0.57	0.05249	0.00216	0.13947	0.00758	0.01953	0.00030	307	92	133	7	125	2
TW1-09	1160	1223	0.95	0.05714	0.00326	0.15876	0.01096	0.01986	0.00027	497	125	150	10	127	2
TW1-10	561	1007	0.56	0.05242	0.00189	0.18869	0.00902	0.02654	0.00036	304	81	176	8	169	2
TW1-11	4320	6172	0.70	0.05028	0.00127	0.13679	0.00505	0.01948	0.00027	208	58	130	5	124	2
TW1-12	903	1749	0.52	0.05052	0.00179	0.14412	0.00680	0.02057	0.00028	219	81	137	6	131	2
TW1-13	2427	4553	0.53	0.05755	0.00130	0.16636	0.00551	0.02087	0.00026	513	49	156	5	133	2
TW1-14	1071	2386	0.45	0.04857	0.00598	0.12710	0.01712	0.01898	0.00026	127	247	121	15	121	2
TW1-15	1180	2317	0.51	0.05639	0.00474	0.14805	0.01422	0.01904	0.00026	468	185	140	13	122	2
TW1-16	477	1108	0.43	0.04877	0.00373	0.13529	0.01202	0.02012	0.00030	137	163	129	11	128	2
TW1-17	3447	8118	0.42	0.05371	0.00114	0.14679	0.00451	0.01947	0.00022	359	47	139	4	124	1
TW1-18	582	1190	0.49	0.05452	0.00222	0.17649	0.00937	0.02304	0.00033	393	90	165	8	147	2
TW1-19	1598	2242	0.71	0.04995	0.00139	0.18467	0.00724	0.02679	0.00036	193	61	172	6	170	2
TW1-20	247	515	0.48	0.06715	0.00619	0.17563	0.01933	0.01897	0.00039	842	185	164	17	121	2
TW1-21	1240	2350	0.53	0.05021	0.00144	0.14930	0.00584	0.02140	0.00026	205	63	141	5	136	2
TW1-22	966	1825	0.53	0.04735	0.00508	0.13154	0.01561	0.02015	0.00030	67	205	125	14	129	2
Andesite sample TW2															
TW2-01	1373	2066	0.66	0.05190	0.00457	0.13968	0.01397	0.01952	0.00028	281	186	133	12	125	2
TW2-02	1175	2296	0.51	0.04752	0.00255	0.13130	0.00808	0.02004	0.00020	75	108	125	7	128	1
TW2-03	1136	2472	0.46	0.04563	0.00153	0.12965	0.00555	0.02047	0.00022	−22	62	124	5	131	1
TW2-04	1036	2022	0.51	0.04759	0.00432	0.12754	0.01277	0.01944	0.00024	79	179	122	12	124	1
TW2-05	515	1439	0.36	0.04778	0.00272	0.13494	0.00911	0.02048	0.00029	88	120	129	8	131	2
TW2-06	1009	2048	0.49	0.05058	0.00179	0.14403	0.00691	0.02053	0.00030	222	80	137	6	131	2
TW2-07	2542	3944	0.64	0.06654	0.00336	0.19318	0.01153	0.02106	0.00023	823	104	179	10	134	1
TW2-08	713	1457	0.49	0.04650	0.00335	0.13034	0.01067	0.02033	0.00027	23	147	124	10	130	2
TW2-09	1332	1403	0.95	0.04629	0.00683	0.11942	0.01921	0.01871	0.00033	13	262	115	17	119	2
TW2-10	1895	3947	0.48	0.05102	0.00407	0.12969	0.01196	0.01844	0.00028	242	175	124	11	118	2
TW2-11	1107	2731	0.41	0.05207	0.00607	0.14423	0.01822	0.02009	0.00022	288	244	137	16	128	1
TW2-12	529	971	0.54	0.05709	0.01140	0.14991	0.03325	0.01904	0.00049	495	390	142	29	122	3
TW2-13	1499	3569	0.42	0.05209	0.00144	0.14902	0.00561	0.02060	0.00024	289	61	141	5	131	2
TW2-14	782	1980	0.39	0.04785	0.00290	0.13394	0.00958	0.02030	0.00028	92	125	128	9	130	2
TW2-15	890	1864	0.48	0.05559	0.01508	0.14307	0.04147	0.01867	0.00039	436	490	136	37	119	2
Andesite sample TW3															
TW3-01	806	1689	0.48	0.04886	0.00155	0.14526	0.00624	0.02142	0.00028	141	71	138	6	137	2
TW3-02	597	1571	0.38	0.05623	0.00373	0.15535	0.01222	0.01998	0.00028	461	142	147	11	128	2
TW3-03	1042	1791	0.58	0.05118	0.00203	0.14606	0.00759	0.02051	0.00029	249	88	138	7	131	2
TW3-04	1113	3497	0.32	0.04918	0.00292	0.13355	0.00918	0.01970	0.00023	156	127	127	8	126	1
TW3-05	1924	6210	0.31	0.05432	0.00175	0.15125	0.00663	0.01994	0.00027	384	69	143	6	127	2
TW3-06	1902	4818	0.39	0.05223	0.00132	0.14189	0.00508	0.01963	0.00024	295	57	135	5	125	2
TW3-07	612	937	0.65	0.04607	0.00249	0.12811	0.00814	0.02017	0.00028	1	109	122	7	129	2
TW3-08	767	1695	0.45	0.04846	0.00207	0.13905	0.00766	0.02112	0.00030	122	95	132	7	135	2
TW3-09	631	1443	0.44	0.04888	0.00172	0.15389	0.00722	0.02293	0.00031	142	80	145	6	146	2
TW3-10	1886	6865	0.27	0.04779	0.00125	0.13028	0.00455	0.01954	0.00020	89	59	124	4	125	1
TW3-11	5699	11606	0.49	0.04932	0.00203	0.14073	0.00694	0.02070	0.00021	163	93	134	6	132	1
TW3-12	868	2026	0.43	0.05275	0.00238	0.15753	0.00885	0.02137	0.00027	318	102	149	8	136	2
TW3-13	1229	3559	0.35	0.05159	0.00233	0.14704	0.00808	0.02067	0.00024	267	103	139	7	132	2
TW3-14	968	2338	0.41	0.04645	0.00126	0.13569	0.00521	0.02113	0.00028	21	54	129	5	135	2
TW3-15	1933	5070	0.38	0.04972	0.00113	0.14985	0.00499	0.02156	0.00027	182	52	142	4	138	2
TW3-16	1283	2025	0.63	0.04429	0.00160	0.12752	0.00600	0.02081	0.00026	−56	74	122	5	133	2
TW3-17	1629	6606	0.25	0.05258	0.00271	0.14587	0.00887	0.02012	0.00022	311	116	138	8	128	1
TW3-18	1906	6340	0.30	0.04910	0.00108	0.13703	0.00403	0.02002	0.00017	153	51	130	4	128	1
TW3-19	2324	7539	0.31	0.04920	0.00185	0.14019	0.00665	0.02067	0.00025	157	85	133	6	132	2
Trachyte sample TW4															
TW4-01	1075	2555	0.42	0.05140	0.00191	0.14370	0.00701	0.02024	0.00027	259	85	136	6	129	2
TW4-02	1518	3281	0.46	0.05051	0.00259	0.13742	0.00844	0.01973	0.00024	219	115	131	8	126	2
TW4-03	864	1881	0.46	0.04871	0.00174	0.13791	0.00632	0.02070	0.00024	134	81	131	6	132	2
TW4-04	853	2128	0.40	0.04824	0.00162	0.13689	0.00597	0.02056	0.00024	111	75	130	5	131	2
TW4-05	834	2027	0.41	0.04729	0.00174	0.13884	0.00658	0.02143	0.00026	64	78	132	6	137	2
TW4-06	815	1889	0.43	0.05328	0.00172	0.15803	0.00692	0.02162	0.00029	341	72	149	6	138	2
TW4-07	927	2054	0.45	0.05362	0.00160	0.15715	0.00639	0.02156	0.00027	355	67	148	6	138	2
TW4-08	590	1493	0.40	0.05008	0.00216	0.15434	0.00853	0.02239	0.00031	199	96	146	8	143	2
TW4-09	700	1461	0.48	0.04951	0.00184	0.14844	0.00731	0.02210	0.00031	172	82	141	6	141	2
TW4-10	523	1395	0.38	0.05770	0.00257	0.17896	0.01020	0.02223	0.00032	518	94	167	9	142	2
TW4-11	1240	3853	0.32	0.04616	0.00126	0.13741	0.00492	0.02154	0.00021	6	52	131	4	137	1

Table 2 (*continued*)

Spots	Th (ppm)	U (ppm)	Th/U	Isotopic ratios ± 1σ						Ages ± 1σ (Ma)					
				$^{207}Pb/^{206}Pb$		$^{207}Pb/^{235}U$		$^{206}Pb/^{238}U$		$^{207}Pb/^{206}Pb$		$^{207}Pb/^{235}U$		$^{206}Pb/^{238}U$	
TW4-12	835	1832	0.46	0.04837	0.00182	0.14783	0.00713	0.02227	0.00027	117	82	140	6	142	2
TW4-13	814	2263	0.36	0.04331	0.00126	0.13187	0.00523	0.02214	0.00027	−107	62	126	5	141	2
TW4-14	1138	3002	0.38	0.04491	0.00128	0.13516	0.00527	0.02190	0.00027	−24	54	129	5	140	2
TW4-15	1299	2943	0.44	0.04246	0.00122	0.13267	0.00521	0.02274	0.00028	−152	63	126	5	145	2
TW4-16	1538	3247	0.47	0.04162	0.00111	0.12420	0.00446	0.02168	0.00023	−198	59	119	4	138	1
TW4-17	496	1057	0.47	0.05162	0.00560	0.15179	0.01865	0.02133	0.00037	269	226	143	16	136	2
TW4-18	1072	1859	0.58	0.04772	0.00217	0.13778	0.00790	0.02115	0.00029	85	95	131	7	135	2
TW4-19	769	1840	0.42	0.04846	0.00156	0.14652	0.00640	0.02191	0.00029	122	71	139	6	140	2
TW4-20	1126	2099	0.54	0.05161	0.00165	0.15514	0.00676	0.02162	0.00029	268	71	146	6	138	2
TW4-21	624	1600	0.39	0.05039	0.00273	0.15180	0.00991	0.02185	0.00029	213	119	144	9	139	2
TW4-22	1069	2351	0.45	0.05162	0.00160	0.15891	0.00654	0.02219	0.00026	269	69	150	6	141	2
TW4-23	867	2051	0.42	0.04965	0.00183	0.15345	0.00737	0.02234	0.00029	179	82	145	6	142	2
TW4-24	601	1493	0.40	0.05006	0.00177	0.16024	0.00764	0.02321	0.00033	198	79	151	7	148	2
Dacite sample TW6															
TW6-01	308	769	0.40	0.04824	0.00340	0.15256	0.01269	0.02294	0.00037	111	143	144	11	146	2
TW6-02	327	848	0.39	0.04809	0.00391	0.14944	0.01418	0.02254	0.00041	104	163	141	13	144	3
TW6-03	332	748	0.44	0.05537	0.00248	0.17930	0.01081	0.02378	0.00043	427	94	167	9	152	3
TW6-04	480	892	0.54	0.07287	0.00490	0.23250	0.01900	0.02305	0.00038	1010	130	212	16	147	2
TW6-05	645	1145	0.56	0.05274	0.00239	0.16197	0.00961	0.02214	0.00036	318	97	152	8	141	2
TW6-06	367	887	0.41	0.05595	0.00241	0.17614	0.01026	0.02312	0.00041	450	90	165	9	147	3
TW6-07	480	1075	0.45	0.05269	0.00244	0.16821	0.01029	0.02318	0.00040	315	100	158	9	148	3
TW6-08	344	896	0.38	0.05511	0.00307	0.17478	0.01288	0.02393	0.00050	417	118	164	11	152	3
TW6-09	222	515	0.43	0.05982	0.00350	0.19578	0.01496	0.02367	0.00049	597	120	182	13	151	3
TW6-10	289	682	0.42	0.05276	0.00395	0.16563	0.01456	0.02277	0.00036	318	166	156	13	145	2
TW6-11	398	910	0.44	0.05221	0.00244	0.15924	0.00960	0.02193	0.00034	295	105	150	8	140	2
TW6-12	362	1016	0.36	0.05037	0.00279	0.16937	0.01212	0.02475	0.00046	212	124	159	11	158	3
TW6-13	405	644	0.63	0.09809	0.01875	0.27247	0.05977	0.02015	0.00062	1588	383	245	48	129	4
TW6-14	320	708	0.45	0.04767	0.00356	0.16358	0.01441	0.02489	0.00043	83	156	154	13	158	3
TW6-15	444	1208	0.37	0.04871	0.00305	0.15126	0.01099	0.02252	0.00028	134	135	143	10	144	2
TW6-16	315	697	0.45	0.05292	0.00287	0.15999	0.01099	0.02291	0.00038	325	121	151	10	146	2
TW6-17	611	977	0.63	0.05418	0.00237	0.17226	0.00980	0.02310	0.00035	379	97	161	8	147	2
TW6-18	269	649	0.41	0.05746	0.00319	0.19090	0.01382	0.02419	0.00047	509	121	177	12	154	3
TW6-19	522	1233	0.42	0.04642	0.00219	0.15075	0.00894	0.02366	0.00033	19	96	143	8	151	2
TW6-20	260	584	0.45	0.06700	0.00346	0.20315	0.01420	0.02364	0.00050	838	106	188	12	151	3
TW6-21	268	604	0.44	0.05540	0.00333	0.16783	0.01323	0.02216	0.00048	428	132	158	12	141	3
TW6-22	190	487	0.39	0.06187	0.00286	0.18456	0.01171	0.02240	0.00045	670	97	172	10	143	3
TW6-23	255	602	0.42	0.06649	0.00288	0.20497	0.01223	0.02259	0.00043	822	88	189	10	144	3
TW6-24	300	637	0.47	0.05221	0.00296	0.15627	0.01152	0.02278	0.00045	295	125	147	10	145	3
Dacite sample TW7															
TW7-01	400	1051	0.38	0.05192	0.00223	0.17034	0.00958	0.02357	0.00036	282	96	160	8	150	2
TW7-02	278	586	0.47	0.06152	0.00360	0.20146	0.01509	0.02445	0.00046	657	123	186	13	156	3
TW7-03	326	822	0.40	0.05131	0.00255	0.18152	0.01162	0.02557	0.00042	255	111	169	10	163	3
TW7-04	540	1224	0.44	0.04764	0.00299	0.15180	0.01140	0.02311	0.00036	81	130	143	10	147	2
TW7-05	379	941	0.40	0.05223	0.00234	0.17581	0.01033	0.02465	0.00040	295	99	164	9	157	3
TW7-06	359	731	0.49	0.05107	0.00388	0.17287	0.01563	0.02455	0.00043	244	164	162	14	156	3
TW7-07	268	633	0.42	0.05979	0.00460	0.20004	0.01872	0.02426	0.00048	596	164	185	16	155	3
TW7-08	307	1001	0.31	0.05016	0.00361	0.16452	0.01391	0.02379	0.00037	203	153	155	12	152	2
TW7-09	328	741	0.44	0.08184	0.00457	0.28541	0.02113	0.02476	0.00052	1242	106	255	17	158	3
TW7-10	434	1341	0.32	0.04820	0.00282	0.16155	0.01112	0.02431	0.00031	109	121	152	10	155	2
TW7-11	296	646	0.46	0.05742	0.00457	0.18849	0.01773	0.02381	0.00041	508	170	175	15	152	3
TW7-12	275	841	0.33	0.06444	0.00294	0.24593	0.01437	0.02833	0.00042	756	93	223	12	180	3
TW7-13	331	840	0.39	0.05420	0.00477	0.18402	0.01849	0.02462	0.00036	379	190	172	16	157	2
TW7-14	273	881	0.31	0.04895	0.00824	0.16390	0.03041	0.02428	0.00054	146	308	154	27	155	3
TW7-15	227	711	0.32	0.05360	0.00467	0.17457	0.01795	0.02362	0.00044	354	193	163	16	150	3
TW7-16	365	906	0.40	0.05508	0.00387	0.19336	0.01616	0.02546	0.00041	415	156	179	14	162	3
TW7-17	391	935	0.42	0.05296	0.00205	0.17588	0.00920	0.02405	0.00038	327	87	165	8	153	2
TW7-18	414	1034	0.40	0.04839	0.00182	0.16059	0.00845	0.02411	0.00042	118	84	151	7	154	3
TW7-19	879	3525	0.25	0.05007	0.00150	0.17204	0.00660	0.02471	0.00024	198	69	161	6	157	2
TW7-20	365	783	0.47	0.05592	0.00220	0.18351	0.01021	0.02422	0.00046	449	87	171	9	154	3
TW7-21	309	739	0.42	0.06347	0.00417	0.21185	0.01732	0.02403	0.00044	724	139	195	15	153	3
TW7-22	340	812	0.42	0.05300	0.00682	0.17899	0.02627	0.02449	0.00054	329	272	167	23	156	3
Andesite sample TW8															
TW8-01	1125	2203	0.51	0.05619	0.00341	0.16326	0.01176	0.02107	0.00028	460	134	154	10	134	2
TW8-02	1019	909	1.12	0.04984	0.01706	0.11710	0.04320	0.01704	0.00052	188	542	112	39	109	3
TW8-03	570	1088	0.52	0.07232	0.00442	0.20447	0.01537	0.02001	0.00032	995	124	189	13	128	2
TW8-04	1582	3329	0.48	0.06681	0.01549	0.16724	0.04185	0.01816	0.00036	832	486	157	36	116	2
TW8-05	4360	3328	1.31	0.04931	0.00434	0.13044	0.01298	0.01918	0.00027	163	186	124	12	122	2
TW8-06	1529	2962	0.52	0.05229	0.00173	0.14603	0.00644	0.02023	0.00026	298	74	138	6	129	2
TW8-07	5300	4777	1.11	0.09986	0.00462	0.26013	0.01521	0.01924	0.00027	1621	84	235	12	123	2
TW8-08	1332	2140	0.62	0.05149	0.00202	0.14112	0.00708	0.01995	0.00025	263	88	134	6	127	2
TW8-09	2602	3713	0.70	0.04858	0.00244	0.13182	0.00779	0.01968	0.00022	128	108	126	7	126	1
TW8-10	884	1722	0.51	0.08699	0.00522	0.25001	0.01818	0.02064	0.00030	1360	114	227	15	132	2

(*continued on next page*)

Table 2 (*continued*)

Spots	Th (ppm)	U (ppm)	Th/U	Isotopic ratios ± 1σ						Ages ± 1σ (Ma)					
				$^{207}Pb/^{206}Pb$		$^{207}Pb/^{235}U$		$^{206}Pb/^{238}U$		$^{207}Pb/^{206}Pb$		$^{207}Pb/^{235}U$		$^{206}Pb/^{238}U$	
TW8-11	403	1120	0.36	0.05133	0.00593	0.13241	0.01748	0.01871	0.00038	255	241	126	16	120	2
TW8-12	327	735	0.44	0.07103	0.00409	0.20122	0.01547	0.02059	0.00046	958	116	186	13	131	3
TW8-13	623	1307	0.48	0.04607	0.00380	0.13120	0.01252	0.02066	0.00040	1	162	125	11	132	3
TW8-14	1807	2568	0.70	0.04660	0.00261	0.13210	0.00859	0.02056	0.00027	29	112	126	8	131	2
TW8-15	427	713	0.60	0.05674	0.00307	0.15016	0.01063	0.01983	0.00038	481	116	142	9	127	2
TW8-16	593	1522	0.39	0.05197	0.00548	0.13746	0.01643	0.01918	0.00032	284	223	131	15	123	2
TW8-17	691	1462	0.47	0.04849	0.00197	0.14405	0.00762	0.02183	0.00031	123	89	137	7	139	2
TW8-18	667	1756	0.38	0.09585	0.00418	0.27422	0.01604	0.02079	0.00036	1545	79	246	13	133	2
TW8-19	348	716	0.49	0.06305	0.00316	0.18313	0.01198	0.02208	0.00039	710	103	171	10	141	2
TW8-20	2341	4672	0.50	0.07166	0.00205	0.20211	0.00825	0.02022	0.00029	976	56	187	7	129	2
TW8-21	740	1435	0.52	0.04921	0.00183	0.13379	0.00653	0.02001	0.00027	158	83	127	6	128	2
Trachyte sample TW9															
TW9-01	1303	4031	0.32	0.05142	0.00134	0.18053	0.00638	0.02529	0.00027	260	58	169	5	161	2
TW9-02	892	1840	0.49	0.05693	0.00295	0.17939	0.01168	0.02303	0.00035	489	112	168	10	147	2
TW9-03	2676	3823	0.70	0.05416	0.00295	0.16182	0.01033	0.02167	0.00025	378	119	152	9	138	2
TW9-04	450	1220	0.37	0.05144	0.00459	0.17670	0.01852	0.02491	0.00047	261	193	165	16	159	3
TW9-05	920	2236	0.41	0.04859	0.00260	0.15388	0.00972	0.02297	0.00028	128	115	145	9	146	2
TW9-06	1128	2505	0.45	0.05102	0.00183	0.15322	0.00727	0.02166	0.00029	242	80	145	6	138	2
TW9-07	976	2051	0.48	0.05026	0.00162	0.14764	0.00648	0.02150	0.00029	207	73	140	6	137	2
TW9-08	469	980	0.48	0.05554	0.00224	0.16844	0.00911	0.02202	0.00035	434	86	158	8	140	2
TW9-09	1115	2383	0.47	0.05034	0.00207	0.15618	0.00829	0.02248	0.00031	211	90	147	7	143	2
TW9-10	1885	2584	0.73	0.04985	0.00236	0.14977	0.00901	0.02183	0.00032	188	103	142	8	139	2
TW9-11	643	1136	0.57	0.05161	0.00251	0.16439	0.01010	0.02363	0.00035	268	106	155	9	151	2
TW9-12	756	1533	0.49	0.04349	0.00236	0.14376	0.01002	0.02402	0.00043	−97	110	136	9	153	3
TW9-13	734	1535	0.48	0.04989	0.00229	0.15813	0.00946	0.02291	0.00037	190	100	149	8	146	2
TW9-14	2037	3262	0.62	0.05164	0.00194	0.16113	0.00787	0.02237	0.00029	270	82	152	7	143	2
TW9-15	718	1985	0.36	0.04770	0.00186	0.14540	0.00727	0.02206	0.00028	84	82	138	6	141	2
TW9-16	1770	2942	0.60	0.05103	0.00164	0.15674	0.00668	0.02216	0.00027	242	70	148	6	141	2
TW9-17	1460	2725	0.54	0.05007	0.00278	0.14485	0.00952	0.02098	0.00026	198	120	137	8	134	2
TW9-18	1202	2413	0.50	0.05190	0.00158	0.15154	0.00612	0.02103	0.00024	281	67	143	5	134	2
TW9-19	662	1606	0.41	0.05116	0.00182	0.15445	0.00737	0.02206	0.00031	248	78	146	6	141	2
TW9-20	544	1326	0.41	0.04767	0.00389	0.14250	0.01316	0.02168	0.00031	83	165	135	12	138	2
TW9-21	405	1007	0.40	0.06385	0.00512	0.20106	0.02151	0.02454	0.00076	737	164	186	18	156	5
TW9-22	1791	2960	0.61	0.05198	0.00357	0.15283	0.01219	0.02132	0.00029	285	148	144	11	136	2
TW9-23	2372	2762	0.86	0.05115	0.00346	0.15245	0.01184	0.02162	0.00026	247	147	144	10	138	2
TW9-24	877	1930	0.45	0.05259	0.00318	0.16482	0.01283	0.02287	0.00046	311	132	155	11	146	3
TW9-25	815	1501	0.54	0.05603	0.00191	0.16766	0.00758	0.02181	0.00028	454	73	157	7	139	2

changes of REE distribution patterns (e.g., Labanieh et al., 2012; Yang et al., 2014a).

Chondrite-normalized REE patterns (Fig. 6a) and primitive mantle-normalized incompatible element diagrams (Fig. 6b) for the intermediate and felsic volcanic rocks show similar patterns, with strong incompatible element enrichment. All the volcanic rocks are characterized by enriched light REE (LREE), relatively flat heavy REE (HREE) profiles (chondrite-normalized La/Yb and Dy/Yb ratios are 7.03–11.5 and 1.05–1.36, respectively) and slightly negative Eu anomalies. They have total REE of the volcanic rocks ranging from 100 to 170 ppm, with La/Sm and La/Yb ratios ranging from 3.93 to 6.72 and from 9.80 to 16.1, respectively (Table 3). Trace element concentrations range from several times primitive mantle for heavy REE and Ti, to several hundred times for large ion lithophile elements (LILE) such as Rb, Ba, Th, U and Pb (Fig. 6b). The mantle-normalized incompatible trace element patterns are distinguished by negative Nb–Ta–Ti and positive Pb anomalies, which are features of magma derived from suprasubduction zones (e.g., Boari et al., 2009; Yang et al., 2014a). Exceptionally, the felsic volcanic rocks have relatively high Rb and Pb concentrations and show more significant Sr and Ti depletion, indicating the variation of their mantle sources. With increasing SiO_2 contents, the lack of decrease in Ni and Cr concentrations as well as the MgO contents decreasing from intermediate to felsic rocks indicates that the intermediate and felsic volcanic rocks from the southern GXM were probably derived from different source regions.

Measured and calculated initial (t = 127 Ma) Sr and Nd isotopic compositions of four felsic volcanic rocks from the Baiyingaolao formation are presented in Table 4. The samples are characterized by a limited range of initial isotope ratios with no correlation with rock type. The felsic rhyolites from the southern GXM have elevated radiogenic $(^{87}Sr/^{86}Sr)_i$ (0.705036–0.709641) and low $(^{143}Nd/^{144}Nd)_i$ (0.512495–0.512586) relative to Bulk Earth (Table 4), with $\varepsilon_{Nd}(t)$ values ranging from 0.30 to 2.08. Compared with previous Sr–Nd isotopic data of the Mesozoic volcanic rocks from both southern and northern GXM, most of the Mesozoic volcanic rocks show the trend of lithospheric mantle melting, except the initial $^{87}Sr/^{86}Sr$ value of sample H13 that was affected by the mixing of old crustal components (Fig. 7a). Similarly, the $\varepsilon_{Nd}(t)$ values of the volcanic rocks also show a trend of mixing between juvenile crust and old crust components, as well as the Phanerozoic A-type granitoids in NE China (Fig. 7b; Wu et al., 2002).

5. Discussion

5.1. Timing of the large-scale volcanism

The volcanic rocks of all four volcanic formations in the southern segment of GXM were traditionally considered to be Late Jurassic to Early Cretaceous, in which the Manketouebo, Manitu and Baiyingaolao formations are Late Jurassic and the Meiletu formation is Early Cretaceous (Zhao et al., 1989; IMBGMR, 1991; Lin et al., 1998). In contrast, recent studies show that the majority of the dated volcanic rocks erupted in the Early Cretaceous, with the basal Manketouebo formation erupted in the Late Jurassic

Table 3
Major oxides (in wt.%) and trace element (in ppm) compositions of the Mesozoic volcanic rocks in the southern GXM.

Sample	TW2-1	TW2-2	TW3-1	TW3-2	TW4-1	TW4-2	TW4-3	TW9-1	TW9-2	H13	H14	H15	H16	H17	H18
Lithology	Andesite	Andesite	Andesite	Andesite	Trachydacite	Trachydacite	Trachydacite	Trachydacite	Trachydacite	Rhyolite	Rhyolite	Rhyolite	Rhyolite	Rhyolite	Rhyolite
SiO_2	61.28	61.25	57.29	57.35	64.39	64.39	64.18	63.69	64.36	70.39	69.94	69.86	68.92	69.62	69.85
TiO_2	0.76	0.77	0.99	0.98	0.61	0.62	0.62	0.76	0.74	0.27	0.29	0.29	0.31	0.28	0.26
Al_2O_3	16.94	16.91	17.23	17.18	16.19	16.22	16.35	16.66	16.53	14.50	14.83	14.95	15.52	14.91	13.84
Fe_2O_{3T}	5.63	5.65	7.07	7.03	4.87	4.83	4.86	5.06	4.75	3.03	2.72	2.81	3.01	3.26	3.26
MnO	0.10	0.10	0.13	0.13	0.08	0.08	0.08	0.06	0.06	0.07	0.07	0.07	0.07	0.07	0.06
MgO	1.89	1.91	3.17	3.27	1.71	1.69	1.70	1.44	1.24	0.43	0.46	0.45	0.45	0.45	0.36
CaO	4.55	4.51	5.11	5.25	3.79	3.81	3.80	3.08	3.06	0.59	0.60	0.74	0.54	0.56	1.61
Na_2O	3.79	3.80	4.58	4.42	4.22	4.22	4.30	4.28	4.24	3.87	3.74	3.69	4.44	3.70	4.15
K_2O	3.81	3.80	1.37	1.30	3.27	3.24	3.24	2.91	2.93	5.99	6.32	6.22	5.76	6.06	5.17
P_2O_5	0.25	0.26	0.30	0.31	0.19	0.19	0.19	0.26	0.26	0.06	0.06	0.06	0.07	0.06	0.06
LOI	0.99	1.03	2.74	2.77	0.68	0.70	0.68	1.79	1.81	0.80	0.96	0.85	0.90	1.02	1.37
ToTal	99.52	99.34	99.66	99.59	99.56	99.31	100.00	99.94	99.69	99.95	99.94	99.92	99.94	99.94	99.94
Sc	15.52	15.72	19.60	20.33	10.05	7.48	9.83	8.24	10.91	7.53	7.42	7.99	8.17	7.07	6.77
Ti	4637	4651	6035	6054	3678	3642	3737	4148	4594	1415	1435	1515	1654	1414	1381
V	79.97	80.31	136.10	135.00	81.74	86.69	72.77	61.87	69.58	24.44	19.56	21.78	21.99	18.18	19.74
Cr	49.39	47.32	36.38	34.14	31.74	29.16	30.12	19.74	25.32	16.00	10.64	10.39	12.41	13.71	14.52
Mn	770	757	953	1011	612	600	591	387	478	468	433	536	480	485	379
Co	8.97	8.94	17.01	17.26	10.05	9.77	9.97	7.36	9.03	2.25	1.70	1.81	1.93	2.04	2.28
Ni	4.91	2.93	4.16	5.82	3.48	3.40	3.51	2.06	2.89	5.38	3.50	3.64	4.09	6.06	5.92
Cu	7.50	7.28	16.74	11.12	7.26	8.22	8.13	8.98	11.72	9.79	7.27	6.63	9.40	9.72	12.46
Zn	73.87	74.38	95.23	88.04	68.91	65.87	68.39	74.44	84.16	59.31	57.12	55.38	52.72	51.93	73.13
Ga	20.26	20.37	20.72	20.98	20.13	19.46	20.24	19.21	20.56	19.79	18.91	19.58	20.22	17.59	23.09
Ge	2.07	2.08	2.17	2.20	1.99	1.87	1.90	1.02	1.96	1.49	1.59	1.84	1.61	1.61	1.38
Rb	98.39	98.23	44.68	44.03	110.90	39.10	111.00	69.85	80.36	216	225	244	211	231	214
Sr	522	520	744	754	483	349	485	425	432	116	119	127	133	122	140
Y	22.12	22.37	18.75	19.01	16.04	14.12	15.66	15.21	16.62	21.60	20.96	22.27	22.47	20.36	20.16
Zr	252	251	132	137	198	217	171	225	255	229	266	247	263	234	216
Nb	8.15	8.20	6.21	6.31	6.18	6.31	6.28	5.04	5.68	9.15	9.40	9.29	10.31	8.85	8.43
Cs	3.22	3.13	5.82	6.10	5.68	4.62	5.65	5.88	6.58	\	\	\	\	\	\
Ba	898	915	609	620	547	380	550	799	784	849	916	954	848	879	974
La	27.39	27.62	20.17	19.77	27.88	16.95	27.94	21.78	22.94	35.33	36.79	35.87	37.03	34.57	34.74
Ce	56.70	56.89	43.83	43.43	55.69	40.86	55.91	45.88	48.19	66.51	70.45	68.40	70.63	64.16	67.35
Pr	7.16	7.23	5.79	5.76	6.66	5.17	6.56	5.92	6.25	8.34	8.79	8.83	9.07	8.13	8.34
Nd	28.24	28.44	24.02	24.01	24.50	20.12	24.21	23.64	24.83	30.54	31.67	32.25	32.92	29.52	30.98
Sm	5.54	5.55	5.00	5.03	4.52	4.01	4.42	4.52	4.82	5.38	5.50	5.66	5.83	5.15	5.18
Eu	1.33	1.33	1.33	1.33	1.03	0.93	1.02	1.22	1.30	0.75	0.74	0.79	0.82	0.73	0.70
Gd	4.88	4.94	4.48	4.50	3.87	3.46	3.78	3.85	4.18	4.85	4.37	4.62	4.92	4.44	4.04
Tb	0.73	0.74	0.67	0.68	0.55	0.52	0.54	0.57	0.61	0.76	0.68	0.72	0.74	0.69	0.61
Dy	4.24	4.23	3.87	3.90	3.18	2.97	3.07	3.19	3.45	4.18	4.12	4.32	4.24	3.97	3.44
Ho	0.88	0.88	0.78	0.78	0.64	0.61	0.62	0.63	0.69	0.85	0.82	0.87	0.85	0.80	0.71
Er	2.41	2.41	2.06	2.05	1.74	1.66	1.68	1.70	1.84	2.43	2.35	2.45	2.39	2.27	2.04
Tm	0.36	0.36	0.30	0.30	0.26	0.26	0.26	0.25	0.27	0.37	0.37	0.38	0.38	0.35	0.32
Yb	2.38	2.37	1.91	1.92	1.77	1.73	1.74	1.61	1.74	2.53	2.52	2.51	2.60	2.36	2.19
Lu	0.37	0.38	0.30	0.30	0.28	0.28	0.28	0.25	0.27	0.39	0.39	0.39	0.40	0.37	0.34
Hf	6.38	6.36	3.73	3.80	5.35	5.95	4.77	5.65	6.39	6.25	7.34	6.80	7.25	6.36	6.03
Ta	0.64	0.63	0.51	0.52	0.80	0.84	0.80	0.43	0.48	0.70	0.74	0.75	0.80	0.70	0.69
Pb	16.84	16.44	12.64	12.46	17.35	15.71	17.41	15.27	13.61	31.70	26.71	32.94	36.28	31.48	26.37
Th	8.72	8.71	5.67	5.69	18.90	14.41	17.97	6.88	7.27	12.44	12.29	12.90	13.12	12.22	10.85
U	2.54	2.46	1.79	1.77	2.60	2.33	2.32	2.38	2.64	3.48	3.40	3.53	3.67	3.32	2.66
Mg#	43.90	44.11	51.09	52.05	44.96	44.92	44.91	39.88	37.88	24.85	28.27	27.18	25.84	24.34	20.47
Eu*	0.78	0.77	0.86	0.85	0.75	0.76	0.76	0.89	0.88	0.45	0.46	0.47	0.47	0.47	0.47
$K_2O + Na_2O$	7.60	7.61	5.95	5.71	7.49	7.46	7.54	7.19	7.17	9.86	10.07	9.92	10.21	9.77	9.33
K_2O/Na_2O	1.01	1.00	0.30	0.29	0.78	0.77	0.75	0.68	0.69	1.55	1.69	1.69	1.30	1.64	1.25

Note: Major element oxide contents are normalized to 100 wt.% on a volatile-free basis. Mg# (Mg-number) = molar Mg × 100/(Mg + Fe^{2+}), calculated assuming FeO/(FeO + Fe_2O_3) = 0.85. Fe_2O_3T = total Fe is given as Fe_2O_3. LOI = Loss on ignition. Eu* is the ratio of chondrite-normalized Eu content to the expected concentration of Eu assuming no anomaly of Eu. The normalization factor for the calculation is from Sun and McDonough (1989).

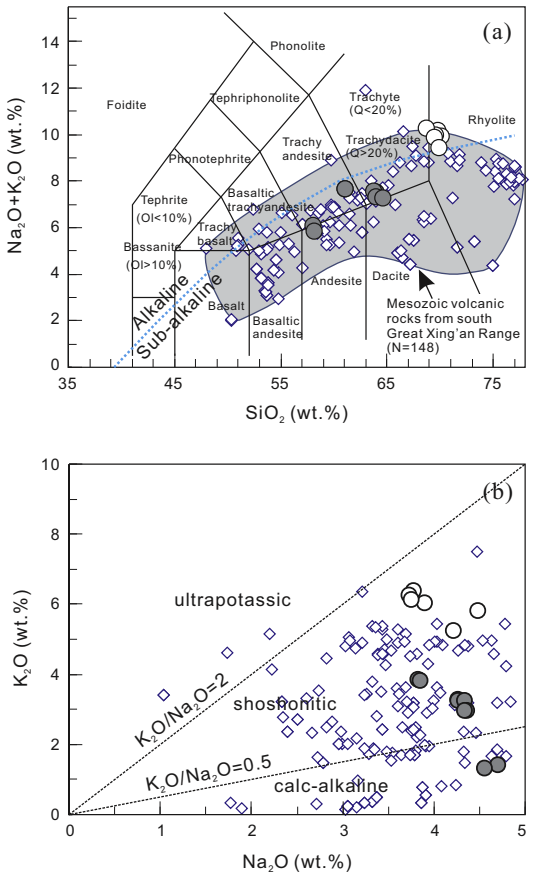

Fig. 5. (a) TAS diagram and (b) relationship between SiO_2 and K_2O content of the volcanic rocks from the southern GXM. Data are referred from literatures (Gao et al., 2005; Ge et al., 2000, 1999; Guo et al., 2001; Li et al., 2013; Lin et al., 2003; Zhang, 2009) and this study.

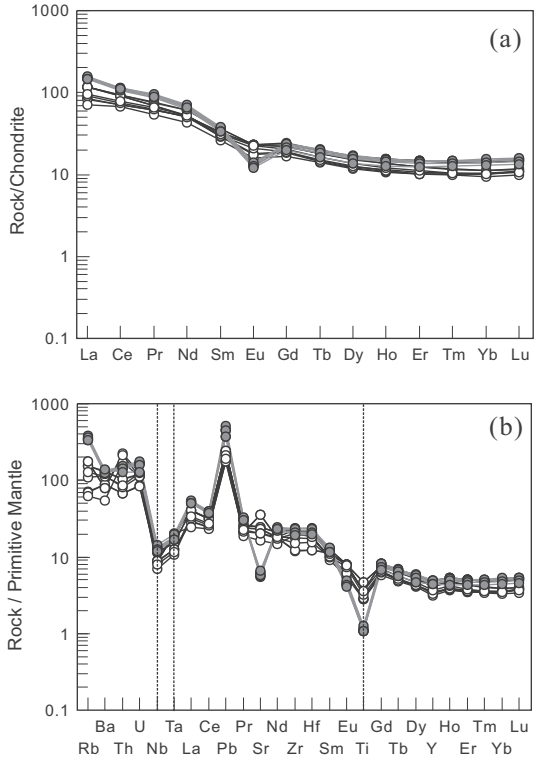

Fig. 6. (a) REE distribution pattern and (b) trace element spider diagrams of the Mesozoic volcanic rocks from the southern GXM. The primary mantle and chondrite normalized data are from Sun and McDonough (1989).

(Zhang et al., 2010 and references therein). Recently high precise age data show large range in crystallization age for the four volcanic formations, indicating that the subdivision and correlation of these volcanic strata needs to be re-evaluated (Wang et al., 2006; Ying et al., 2010; Zhang et al., 2010). According to our data and compilation in Fig. 2, volcanic rocks from the lowermost Manketouebo Formation, show a large age range from 174 ± 4 Ma to 120 ± 5 Ma, the overlying Manitu Formation from 156 ± 1 Ma to 125 ± 1 Ma, the succeeding Baiyingaolao Formation from 139 ± 2 Ma to 124 ± 1 Ma and the uppermost Meiletu Formation from 136 ± 2 Ma to 122 ± 2 Ma. This is clearly impossible in a reasonable stratigraphic sequence and indicates that previous correlations across the area are incorrect (Zhang et al., 2010). Only the upper Meiletu Formation shows a consistent range of younger ages. Nevertheless, the large rang in crystallization age of the volcanic rocks in the four volcanic formations show a climax in the Early Cretaceous, consistent with the giant igneous event recognized in other parts of NE China (Jahn, 2004; Wu et al., 2005; Yang and Li, 2008; Yang et al., 2014b).

Compared with the volcanic strata in the southern segment of GXM, the volcanic rocks in the northern region have relatively high contents of alkalis and much more mafic in compositional for the basalt and basaltic andesite of the Tamulangou Formation (Zhang et al., 2008a). The initiation of volcanism across both the northern and southern regions of GXM was considered to be synchronous in the Late Jurassic (Zhang et al., 2008a, 2010). The presented 127 analyses of eight samples in this study yield zircon U–Pb ages ranging from 163 ± 3 Ma to 109 ± 3 Ma with a weighted mean at 135 ± 2 Ma (Table 2), consistent with the age distribution of the giant igneous event in the whole GXM (Fig. 8). However, the age data indicate that Jurassic volcanic rocks form a relatively subordinate proportion of the giant igneous event, although erosion prior to eruption of the Early Cretaceous rocks may have contributed to this. Therefore, the extensive volcanism in the southern GXM is an important component of the giant Cretaceous igneous event in NE China (Wu et al., 2005).

5.2. Petrogenesis of the calc-alkaline and shoshonitic rocks

5.2.1. Subduction-modified mantle source

Mantle metasomatism and partial melting are important geological processes in the deep Earth, whereas partial melting of subducted crustal components is the most important agent for generating mantle metasomatism (Zhang, 2005; Sun et al., 2013a). Many studies have documented that the metasomatism of mantle source by subduction is predominantly constrained slab melting and/or slab devolatization (Turner and Hawkesworth, 1997; Gorman et al., 2006; Labanieh et al., 2012; Yang et al., 2014a). The presented chemical compositions of the calc-alkaline and shoshonitic rocks from the southern GXM are consistent with a mantle source affected by slab dehydration rather than melting of subducted sediments.

Dehydration of subducted slab will occur before melting due to their P–T profiles (Syracuse and Abers, 2006; Syracuse et al., 2010), and the resulting fluids will play a critical role in the fertilization and melting of the mantle wedge (Kogiso et al., 1997; Gorman et al., 2006; Zhang et al., 2007; Sun et al., 2014). The relative immobility of some incompatible elements (e.g., HFSE) in aqueous fluids has long been used to distinguish between the roles of melts and fluids as metasomatising agents (Labanieh et al., 2012; Yang et al., 2014a). The Th budget in subduction-related volcanic rocks

Table 4
Sr and Nd isotopic compositions of the felsic shoshonite in the southern GXM.

Sample	$^{87}Rb/^{86}Sr$	$^{87}Sr/^{86}Sr$	2σ	$(^{87}Sr/^{86}Sr)_i$	$^{147}Sm/^{144}Nd$	$^{143}Nd/^{144}Nd$	2σ	$(^{143}Nd/^{144}Nd)_i$	$\varepsilon_{Nd}(t)$	$T_{DM,2}$(Ma)
H13	5.3765	0.719040	0.000016	0.709641	0.1065	0.512581	0.000011	0.512495	0.30	892
H14	5.4901	0.714633	0.000020	0.705036	0.1049	0.512670	0.000008	0.512586	2.08	747
H16	4.5950	0.714733	0.000013	0.706700	0.1071	0.512605	0.000013	0.512519	0.76	854
H18	4.4364	0.713007	0.000016	0.705252	0.1012	0.512662	0.000007	0.512581	1.98	755

Note: Initial values were calculated by using the age of 127 Ma.

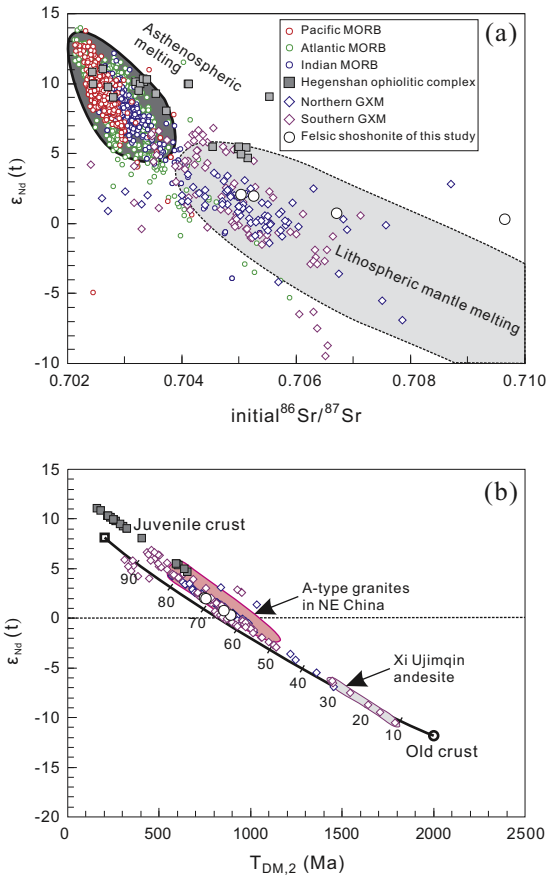

Fig. 7. (a) $\varepsilon_{Nd}(t)$ vs. initial $^{87}Sr/^{86}Sr$ diagram of the Mesozoic volcanic rocks in the southern GXM, compared with MORBs from the PETDB database (http://www.earthchem.org/petdb) and Mesozoic volcanic rocks in both Northern Great Xing'an Mountains (NGXM) and Southern Great Xing'an Mountains (SGXM) in literature (Guo et al., 2010). (b) $\varepsilon_{Nd}(t)$ vs. T_{DM2} (two-stage model ages) diagram of the Mesozoic volcanic rocks in the southern GXM. The curve represents the mixing proportions between the Juvenile crust and old crust components, according to Wu et al. (2002). Symbol size is larger than analytical error (2σ).

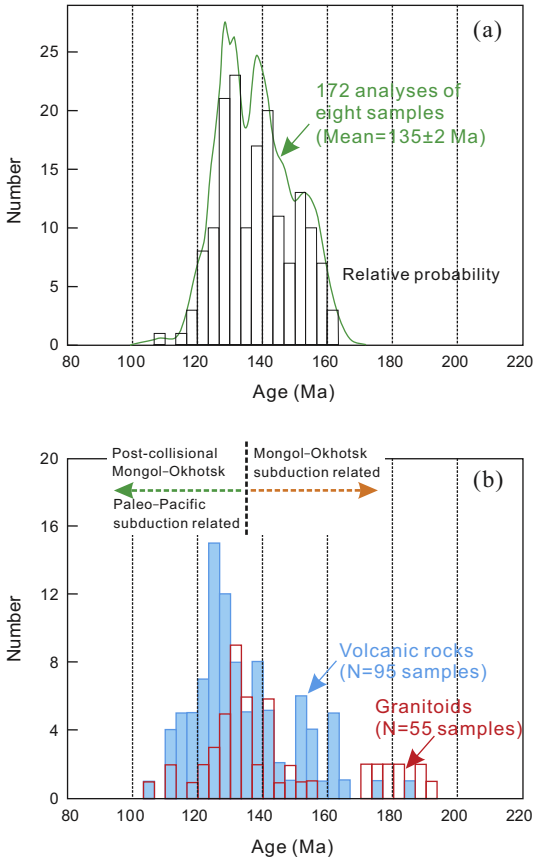

Fig. 8. (a) Age distribution for 127 analyses of the eight selected volcanic rocks from the southern GXM. (b) Compilation of age data of volcanic rocks and granites from the whole GXM (modified after Zhang et al. (2010)).

is usually considered to be controlled by sediment recycling (Plank and Langmuir, 1998). High Th concentrations, Th/Nb and La/Sm ratios in subduction-related lavas have been interpreted to have been caused by the incorporation of recycled sediments (Avanzinelli et al., 2009; Labanieh et al., 2012). In contrast, subduction-related fluids are generally considered enriched in elements such as Ba, Pb, Rb, U and Sr and depleted in Th, Nb, Ta, Hf, Ti and REE (Brenan et al., 1995; Ayers et al., 1997; Kessel et al., 2005), which are consistent with the trace elements distribution patterns for the volcanic rocks in the southern GXM (Fig. 6b). Labanieh et al. (2012) attributed the high Ba/Th and $^{143}Nd/^{144}Nd$ ratios and low La/Sm and $^{87}Sr/^{86}Sr$ ratios in arc lavas on Martinique to the influence of aqueous fluids formed by slab dehydration, whereas, the lavas with low Ba/Th and $^{143}Nd/^{144}Nd$ ratios and high La/Sm and $^{87}Sr/^{86}Sr$ ratios are attributed to the influence of hydrous melts by melting of slab sediments. In the southern GXM, the volcanic rocks show the characteristics of magma from the active continental margin, with high Ba/Th ratios and low $^{87}Sr/^{86}Sr$ and La/Sm ratios (Figs. 7 and 9), suggesting that the mantle source are predominately influenced by slab dehydration rather than melting of sediments.

5.2.2. Origin of the intermediate calc-alkaline and shoshonitic magma

K-rich igneous rocks are usually considered to have formed from the partial melting of amphibole/phlogopite veins or their host mantle wedge, with their K concentrations controlled by the abundance of amphibole/phlogopite in the vein network, the amounts of mantle component involved, and the degree of partial melting (Avanzinelli et al., 2009; Conticelli et al., 2009a, 2009b;

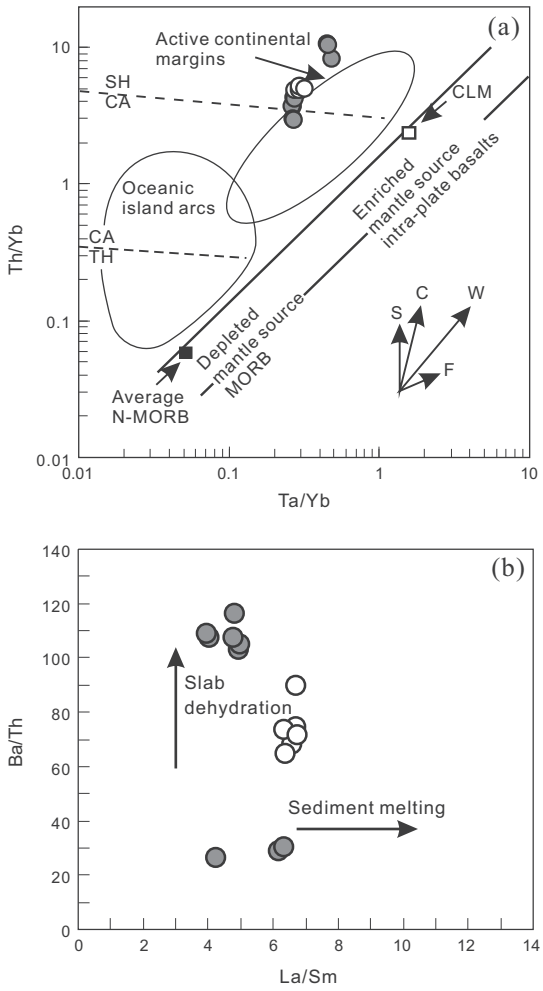

Fig. 9. (a) Th/Yb vs. Ta/Yb diagram (after Pearce (1983)), with SH, shoshonitic basalt; CA, calc-alkaline basalts; TH, tholeiitic basalt; S, subduction zone enrichment; C, crustal contamination; W, within plate enrichment; F, fractional crystallization. (b) Ba/Th vs. La/Sm diagram (after Labanieh et al. (2012)), showing the source nature of the Mesozoic volcanic rocks in the southern GXM.

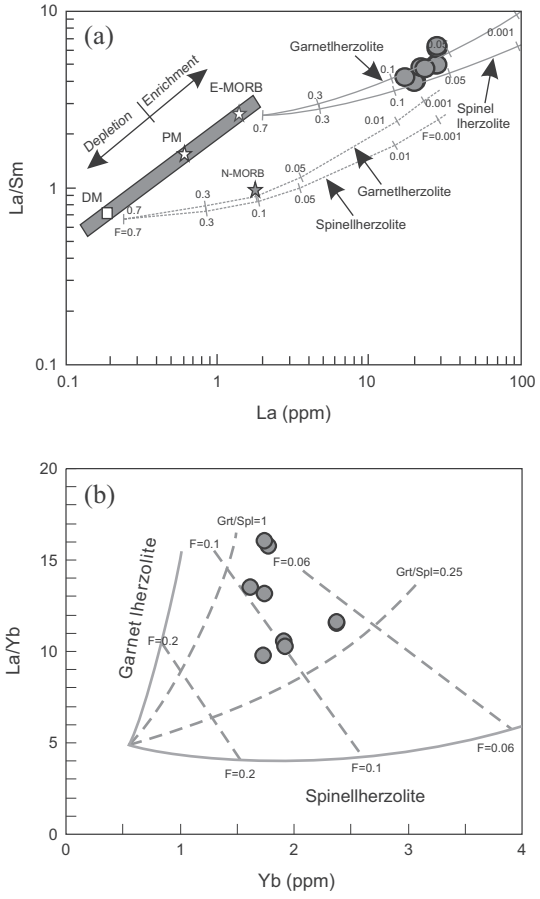

Fig. 10. (a) La/Sm versus La and (b) La/Yb versus Yb diagrams, showing the source and fractionation characteristics of the intermediate volcanic rocks from the southern GXM (after Zhu et al. (2009) and Yang et al. (2012)).

Yang et al., 2014a). Amphiboles from mantle xenoliths display relatively high abundances of K, Sr, LREE, HFSE, and Ba in some cases, but very low abundances of Rb and Th (Ionov and Hofmann, 1995; Chazot et al., 1996). In contrast, phlogopites are rich in K, Sr, Ba, and Rb, but have very low concentrations of REE, HFSE and Th. The K/Rb ratios of phlogopites vary from 40 to 400, whereas those of amphiboles and amphibole-bearing melt are generally greater than 1100 (Hart and Aldrich, 1967; Chakrabarti et al., 2009). The volcanic rocks in the southern GXM have relatively low K/Rb ratios (203–693), as well as relatively low REE and HFSE abundances, indicating that phlogopites are the dominant hydrous minerals in the source region. Besides, the variations in both lithology and composition for the intermediate volcanic rocks of calc-alkaline and shoshonitic were induced by fractionation crystallization of plagioclase in majority and clinopyroxene in minority.

In addition, the La/Sm and La/Yb ratios of the volcanic rocks are 3.93–6.72 and 9.80–16.1, respectively, which demonstrate that all the calc-alkaline and shoshonitic rocks were originated by the batch partial melting of spinel and garnet peridotite (e.g., Genc and Tuysuz, 2010; Yang et al., 2012). The partial melting curves that coincide with the compositions of the volcanic rocks imply <10% partial melting of an enriched mantle source based upon La abundance and La/Sm ratios (Fig. 10a). Furthermore, the Dy/Yb ratio is an important geochemical index for distinguishing partial melting between the spinel and garnet stability fields of an amphibole- and/or phlogopite-bearing lherzolite (Duggen et al., 2005; Jiang et al., 2009). Partial melting in the garnet stability field generally leads to high Dy/Yb ratios (>2.5), whereas melting in the spinel stability field would produce melts with low Dy/Yb ratios (<1.5). The presented volcanic rocks have intermediate Dy/Yb ratios ranging from 1.58 to 2.03, which implies that the source mantle contains both garnet-facies and spinel-facies lherzolite (e.g., Duggen et al., 2005). The La/Yb ratios of igneous rocks are sensitive to basalt source mineralogy, because Yb is typically more compatible in garnet than in clinopyroxene or spinel (Luhr et al., 1995). The Yb concentrations and La/Yb ratios suggest that the mineral ratios of garnet/spinel in the source region are all less than 0.25. In the La/Yb vs. Yb modal diagram, all volcanic rocks plot in the spinel–garnet lherzolite field (Fig. 10b). Consequently the magma source of the volcanic rocks could be produced by relatively low degree partial melting ($F < 0.1$) of garnet–spinel lherzolite (Fig. 10b). Thus, all volcanic rocks from the GXM were likely to derive from partial melting of the garnet–spinel lherzolite transitional field (<27 kbar, Klemme and O'Neill, 2000).

5.2.3. Origin of the felsic shoshonitic magma

It is generally accepted that direct melting of the mantle could not have produced the felsic members (Campbell et al., 2014 and references therein). In addition, the lack of decrease in Ni and Cr concentrations with increasing SiO_2 and decreasing MgO contents from intermediate to felsic rocks in the southern GXM precludes the possibility that the felsic members were derived by fractional

crystallization from the intermediate members (Table 3). It is suggested that, therefore, the felsic shoshonite in the southern GXM probably have different source regions from the associated mantle-derived intermediate volcanic rocks.

The felsic rhyolite are also documented closely associated with the widely distributed A-type and I-type granites in NE China (Wu et al., 2002 and references therein), including the Cretaceous Baerzhe alkaline granite (Jahn et al., 2001; Yang et al., 2014b). Base on the similar Sr/Nd isotopic characteristics, Wu et al. (2002) proposed that both the A-type and I-type granites are derived from the same mixed source with proportions of juvenile and ancient crustal components. If assumed underplated mafic crust has a concentration of Nd about 15 ppm according to Wu et al. (2002), the two-component mixing model suggest that the rhyolite along with the A-type granites in NE China are dominated by new, mantle-derived juvenile material (Fig. 7b). In this respect, the Hegenshan ophiolitic complex represents a juvenile source and the Xi Ujimqin andesite represents a predominantly old crustal source (Fig. 7b), so far reported in the southern GXM (Guo et al., 2010). Therefore, the felsic shoshonitic magma in the southern GXM is plausibly crustal derived. It is consistent with some previous documentation that felsic shoshonite can be derived by partial melting of the lower crust, following underplating by mantle-derived magma, e.g., post-collisional shoshonitic rocks from the East African Orogen (Kuster and Harms, 1998) and the Kunlun Orogenic Belt (Jiang et al., 2002).

5.3. Geodynamic implications

NE China is the eastern part of the CAOB that formed by the amalgamation of multiple micro-continental blocks and arcs in Paleozoic (Li, 2006 and references therein). During the Late Paleozoic–Early Mesozoic, the final closure of the Paleo-Asian Ocean indicated the completion of the CAOB evolutionary (Xiao et al., 2003; Jahn, 2004; Chen et al., 2009; Wang et al., 2015). After that, the whole NE Asia was subsequent in the Mongol–Okhotsk tectonic system and circum-Pacific tectonic system in the Late Mesozoic (Metelkin et al., 2010; Sun et al., 2013b). Besides the GXM, Late Mesozoic igneous rocks are also widespread in other parts of NE China (Fig. 1a), including the Lesser Xing'an Mountains, the eastern part of the Jilin–Heilongjiang Provinces, the Songliao Basin, the Zhangguangcai Range, and the Jiamusi Massif (Wu et al., 2005; Wang et al., 2006; Zhang et al., 2010). However, it is a contentious issue that these intensively magmatic activities in Late Mesozoic were predominantly controlled by whether the Mongol–Okhotsk tectonic system or the western-Pacific tectonic system (Fan et al., 2003; Gao et al., 2005; Wang et al., 2006; Guo et al., 2010; Zhang et al., 2010). The generation of the calc-alkaline and shoshonitic rocks reported here favors an explanation by partial melting of thickened lithospheric mantle and lower crust in extensional setting induced by tectonic regime transition rather than mantle plume activity or some other intraplate process.

The question remains as to what can cause such a tectonic transition to induce the large-scale igneous event in NE China. Previous paleomagnetic reconstructions indicated that the Mongol–Okhotsk Ocean was still not closed completely before the end of the Jurassic, and that the scissors-like closure was considered to be from west to east (Enkin et al., 1992; Metelkin et al., 2010). During the gradual closure, the western part of this ocean was at the Early/Middle Jurassic boundary (Zorin, 1999), whereas, the final collision of the eastern part was occurred in the Early Cretaceous (Metelkin et al., 2010), and then led to the complete collision of Siberia and Mongolia–China blocks (Fig. 11). Subsequent crustal shortening and thickening was resulted from the subduction and demission of the Mongol–Okhotsk Ocean. Partial melting of the thickened lower crust and underlying lithospheric mantle induced by convecting asthenosphere or delamination was proposed critical to the generation of high-Mg andesitic magma at 136 ± 2 Ma (Li et al., 2013). After that, large-scale volcanism was erupted in NE China during Early Cretaceous with a peak of about 125 Ma (Fig. 7b), which was consistent with the time of lithospheric thinning in the eastern North China Craton that resulting in the removal of >120 km of lithosphere induced by the subduction of the paleo-Pacific ocean plate (Menzies et al., 1993; Meng, 2003; Wu et al., 2005; Lin et al., 2008).

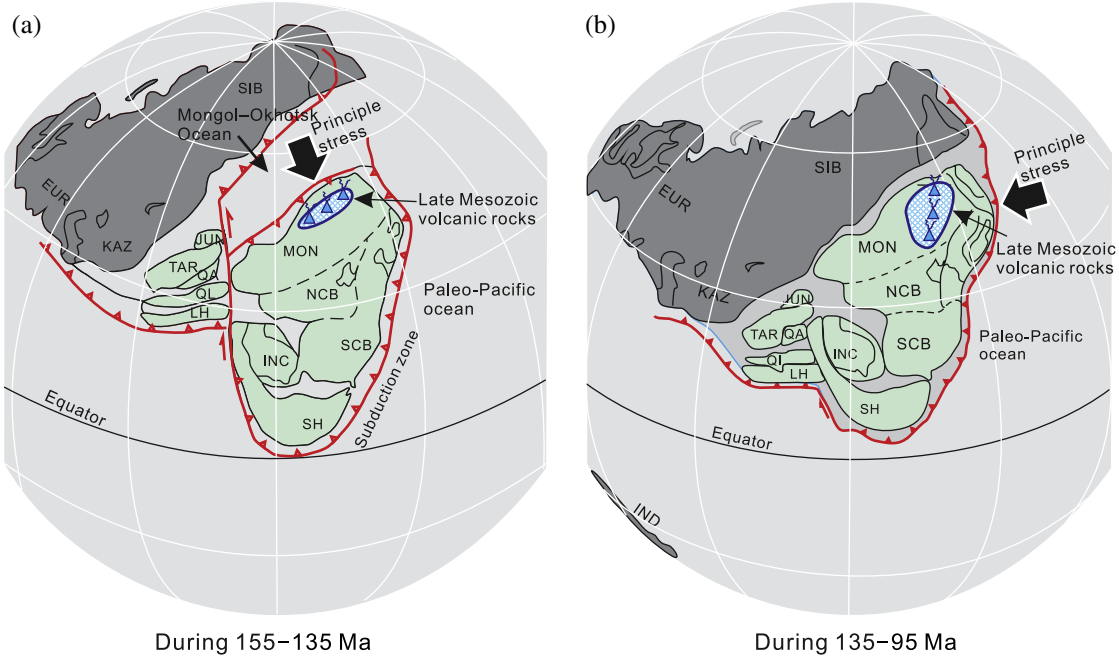

Fig. 11. Late Mesozoic paleoreconstruction of Asian blocks and adjacent Siberia (after Enkin et al. (1992)), showing the dominantly regional principle stress directions (the dark arrows) that transferred from southward (a) to westward (b). Abbreviations refer to major tectonic divisions: EUR, Europe; INC, Indo-China; IND, India; JUN, Junggar; KAZ, Kazakhstan; LH, Lhasa; MON, Mongolian; NCB, north China; QA, Qiadam; QI, Qiangtang; SCB, south China; SH, Shan Thai; SIB, Siberian; and TAR, Tarim.

In this scenario, with continued southward subduction of the Mongol–Okhotsk Ocean, the rheologically heterogeneous lithospheric mantle would become over-thickened in the Late Jurassic. After the closure of the Mongol–Okhotsk Ocean, the tectonic regime of NE China was dominantly controlled by the subduction of the paleo-Pacific Ocean plate. It is means that the NE China was subsequent in a back-arc extensional setting of the western-Pacific tectonic system in the Early Cretaceous, during which the regional north–south stress transformed from compression to extension (Fig. 11). Because of the gravitational instability and mantle convection, the over-thickened lithospheric mantle the started to delaminating and was gradually replaced by hotter asthenosphere. Consequently, the upwelling of the asthenosphere resulted in partial melting of the residual part of lithospheric mantle metasomatized during the Mongol–Okhotsk Ocean seafloor subduction and thickened lower crust, generating the large-scale volcanism and granitoids in GXM and adjacent regions of NE China during Early Cretaceous. The poloidal mantle flow around the delaminated mantle lithosphere may be responsible for the formation of the Songliao back-arc basin and the extensive lithospheric thinning in the eastern China.

6. Conclusions

(1) A systematic geochronological study of the calc-alkaline and shoshonitic rocks in the southern GXM indicates that they were erupted in the Late Jurassic and Early Cretaceous, ranging in age from 154 Ma to 127 Ma. However, they are dominantly Early Cretaceous in age.
(2) The intermediate calc-alkaline and shoshonitic magma resulted from partial melting of metasomatized mantle lithosphere under garnet–spinel facies conditions, whereas the felsic shoshonitic magma was resulted from the partial melting of thickened lower crust. Both the crust and lithosphere mantle has experienced extensive thickening and multiple metasomatic events during the Mongol–Okhotsk Ocean seafloor subduction in Jurassic. Ancient crustal components have contributed to the extensive magmatism in NE China.
(3) The extensional tectonic regime resulted in the large-scale igneous event in NE China were induced by the delamination of lower part of the over-thickened mantle lithosphere. We propose a hypothesis that the large-scale magmatism in Early Cretaceous was probably triggered by regional stress steering from compression to extension that induced by the tectonic transformation from southward Mongol–Okhotsk Ocean subduction to westward paleo-Pacific Ocean subduction.

Acknowledgments

This study was financially supported by the National Natural Science Foundation of China (NSFC) Grants 41472062, 41173040 and 40872066. We are grateful to Wenjiao Xiao for editorial handling and the two anonymous reviewers for constructive comments that helped improve the manuscript substantially. We are also grateful to Dr. Congyin Li and Xianglin Tu for the help with LA-ICPMS analyses, Dr. Lingjun Zeng, Shuang Yan and Ms. Guangqian Hu for determination of elemental and isotopic compositions, respectively. This is GIGCAS contribution No. IS-1994.

References

Altherr, R., Topuz, G., Siebel, W., Sen, C., Meyer, H.P., Satir, M., Lahaye, Y., 2008. Geochemical and Sr–Nd–Pb isotopic characteristics of Paleocene plagioleucitites from the Eastern Pontides (NE Turkey). Lithos 105, 149–161.
Avanzinelli, R., Lustrino, M., Mattei, M., Melluso, L., Conticelli, S., 2009. Potassic and ultrapotassic magmatism in the circum-Tyrrhenian region: significance of carbonated pelitic vs. pelitic sediment recycling at destructive plate margins. Lithos 113, 213–227.
Ayers, J.C., Dittmer, S.K., Layne, G.D., 1997. Partitioning of elements between peridotite and H_2O at 2.0–3.0 GPa and 900–1100 °C, and application to models of subduction zone processes. Earth Planet. Sci. Lett. 150, 381–398.
Black, L.P., Kamo, S.L., Allen, C.M., Aleinikoff, J.N., Davis, D.W., Korsch, R.J., Foudoulis, C., 2003. TEMORA 1: a new zircon standard for Phanerozoic U–Pb geochronology. Chem. Geol. 200, 155–170.
Boari, E., Avanzinelli, R., Melluso, L., Giordano, G., Mattei, M., De Benedetti, A.A., Morra, V., Conticelli, S., 2009. Isotope geochemistry (Sr–Nd–Pb) and petrogenesis of leucite-bearing volcanic rocks from "Colli Albani" volcano, Roman Magmatic Province, Central Italy: inferences on volcano evolution and magma genesis. Bull. Volcanol. 71, 977–1005.
Brenan, J.M., Shaw, H.F., Ryerson, F.J., Phinney, D.L., 1995. Mineral-aqueous fluid partitioning of trace-elements at 900 °C and 2.0 GPa – constraints on the trace-element chemistry of mantle and deep-crustal fluids. Geochim. Cosmochim. Acta 59, 3331–3350.
Campbell, I.H., Stepanov, A.S., Liang, H.Y., Allen, C.M., Norman, M.D., Zhang, Y.Q., Xie, Y.W., 2014. The origin of shoshonites: new insights from the Tertiary high-potassium intrusions of eastern Tibet. Contrib. Miner. Petrol. 167, 1–22.
Chakrabarti, R., Basu, A.R., Santo, A.P., Tedesco, D., Vaselli, O., 2009. Isotopic and geochemical evidence for a heterogeneous mantle plume origin of the Virunga volcanics, Western rift, East African Rift system. Chem. Geol. 259, 273–289.
Chazot, G., Menzies, M.A., Harte, B., 1996. Determination of partition coefficients between apatite, clinopyroxene, amphibole, and melt in natural spinel lherzolites from Yemen: implications for wet melting of the lithospheric mantle. Geochim. Cosmochim. Acta 60, 423–437.
Chen, B., Jahn, B.M., Tian, W., 2009. Evolution of the Solonker suture zone: constraints from zircon U–Pb ages, Hf isotopic ratios and whole-rock Nd–Sr isotope compositions of subduction-and collision-related magmas and forearc sediments. J. Asian Earth Sci. 34, 245–257.
Conticelli, S., Guarnieri, L., Farinelli, A., Mattei, M., Avanzinelli, R., Bianchini, G., Boari, E., Tommasini, S., Tiepolo, M., Prelevic, D., Venturelli, G., 2009a. Trace elements and Sr–Nd–Pb isotopes of K-rich, shoshonitic, and calc-alkaline magmatism of the Western Mediterranean Region: genesis of ultrapotassic to calc-alkaline magmatic associations in a post-collisional geodynamic setting. Lithos 107, 68–92.
Conticelli, S., Marchionni, S., Rosa, D., Giordano, G., Boari, E., Avanzinelli, R., 2009b. Shoshonite and sub-alkaline magmas from an ultrapotassic volcano: Sr–Nd–Pb isotope data on the Roccamonfina volcanic rocks, Roman Magmatic Province, Southern Italy. Contrib. Miner. Petrol. 157, 41–63.
Duggen, S., Hoernle, K., Van den Bogaard, P., Garbe-Schonberg, D., 2005. Post-collisional transition from subduction- to intraplate-type magmatism in the westernmost Mediterranean: evidence for continental-edge delamination of subcontinental lithosphere. J. Petrol. 46, 1155–1201.
Enkin, R.J., Yang, Z.Y., Chen, Y., Courtillot, V., 1992. Paleomagnetic constraints on the geodynamic history of the major blocks of China from the Permian to the present. J. Geophys. Res. – Solid Earth 97, 13953–13989.
Fan, W.M., Guo, F., Wang, Y.J., Lin, G., 2003. Late Mesozoic calc-alkaline volcanism of post-orogenic extension in the northern Da Hinggan Mountains, northeastern China. J. Volcanol. Geoth. Res. 121, 115–135.
Gao, X., Feng, G., Fan, W., Li, C., Li, X., 2005. Origin of late Mesozoic intermediate-felsic volcanic rocks from the northern Da Hinggan Mountain, NE China. Acta Petrol. Sin. 21, 737–748 (in Chinese with English abstract).
Ge, W., Lin, Q., Sun, D., Wu, F., Won, C., Lee, M., Jin, M., Yun, S., 1999. Geochemical characteristics of the Mesozoic basalts in Da Hinggan Ling: evidence of the mantle–crust interaction. Acta Petrol. Sin. 15, 396–407 (in Chinese with English abstract).
Ge, W., Lin, Q., Sun, D., Wu, F., Li, X., 2000. Geochemical research into origins of two types of Mesozoic rhyolites in Daxing'an Ling. Earth Sci. – J. China Univ. Geosci. 36, 172–178 (in Chinese with English abstract).
Genc, S.C., Tuysuz, O., 2010. Tectonic setting of the Jurassic bimodal magmatism in the Sakarya Zone (Central and Western Pontides), Northern Turkey: a geochemical and isotopic approach. Lithos 118, 95–111.
Gorman, P.J., Kerrick, D.M., Connolly, J.A.D., 2006. Modeling open system metamorphic decarbonation of subducting slabs. Geochem. Geophys. Geosyst. 7.
Guo, F., Fan, W., Wang, Y., Lin, G., 2001. Petrogenesis of the late mesozoic bimodal volcanic rocks in the southern Da Hinggan Mts, China. Acta Petrol. Sin. 17, 161–168 (in Chinese with English abstract).
Guo, F., Fan, W.M., Gao, X.F., Li, C.W., Miao, L.C., Zhao, L.A., Li, H.X., 2010. Sr–Nd–Pb isotope mapping of Mesozoic igneous rocks in NE China constraints on tectonic framework and Phanerozoic crustal growth. Lithos 120, 563–578.
Hart, S.R., Aldrich, L.T., 1967. Fractionation of potassium/rubidium by amphiboles: implications regarding Mantle composition. Science 155, 325–327.
Hermann, J., Rubatto, D., 2009. Accessory phase control on the trace element signature of sediment melts in subduction zones. Chem. Geol. 265, 512–526.
IMBGMR (Inner Mongolia Bureau of Geology and Mineral Resources), 1991. Regional Geology of Nei Mongol (Inner Mongolia) Autonomous Region. Geological Publishing House, Beijing, p. 725 (in Chinese with English abstract).
Ionov, D.A., Hofmann, A.W., 1995. Nb–Ta-rich mantle amphiboles and micas – implications for subduction-related metasomatic trace-element fractionations. Earth Planet. Sci. Lett. 131, 341–356.
Jahn, B.M., 2004. The central Asian orogenic belt and growth of the continental crust in the phanerozoic. Aspects Tectonic Evol. China 226, 73–100.

Jahn, B.M., Wu, F.Y., Capdevila, R., Martineau, F., Zhao, Z.H., Wang, Y.X., 2001. Highly evolved juvenile granites with tetrad REE patterns: the Woduhe and Baerzhe granites from the Great Xing'an Mountains in NE China. Lithos 59, 171–198.

Jiang, Y.H., Jiang, S.Y., Ling, H.F., Zhou, X.R., Rui, X.J., Yang, W.Z., 2002. Petrology and geochemistry of shoshonitic plutons from the western Kunlun orogenic belt, Xinjiang, northwestern China: implications for granitoid geneses. Lithos 63, 165–187.

Jiang, Y.H., Jiang, S.Y., Dai, B.Z., Liao, S.Y., Zhao, K.D., Ling, H.F., 2009. Middle to late Jurassic felsic and mafic magmatism in southern Hunan province, southeast China: implications for a continental arc to rifting. Lithos 107, 185–204.

Kessel, R., Schmidt, M.W., Ulmer, P., Pettke, T., 2005. Trace element signature of subduction-zone fluids, melts and supercritical liquids at 120–180 km depth. Nature 437, 724–727.

Klemme, S., O'Neill, H.S., 2000. The near-solidus transition from garnet lherzolite to spinel lherzolite. Contrib. Miner. Petrol. 138, 237–248.

Kogiso, T., Tatsumi, Y., Nakano, S., 1997. Trace element transport during dehydration processes in the subducted oceanic crust. 1. Experiments and implications for the origin of ocean island basalts. Earth Planet. Sci. Lett. 148, 193–205.

Kuster, D., Harms, U., 1998. Post-collisional potassic granitoids from the southern and northwestern parts of the Late Neoproterozoic East African Orogen: a review. Lithos 45, 177–195.

Labanieh, S., Chauvel, C., Germa, A., Quidelleur, X., 2012. Martinique: a clear case for sediment melting and slab dehydration as a function of distance to the trench. J. Petrol.

Lebas, M.J., Lemaitre, R.W., Streckeisen, A., Zanettin, B., 1986. A chemical classification of volcanic-rocks based on the total alkali silica diagram. J. Petrol. 27, 745–750.

Li, J.Y., 2006. Permian geodynamic setting of Northeast China and adjacent regions: closure of the Paleo-Asian Ocean and subduction of the Paleo-Pacific Plate. J. Asian Earth Sci. 26, 207–224.

Li, X.H., Qi, C.S., Liu, Y., Liang, X.R., Tu, X.L., Xie, L.W., Yang, Y.H., 2005. Petrogenesis of the Neoproterozoic bimodal volcanic rocks along the western margin of the Yangtze Block: new constraints from Hf isotopes and Fe/Mn ratios. Chin. Sci. Bull. 50, 2481–2486.

Li, Y.F., Sun, S.L., Gao, X.Y., 2013. Laser $^{40}Ar/^{30}Ar$ dating and geochemistry of the high-$Mg^{\#}$ volcanic rocks from the Tuquan basin in central Daxinganling. Geol. Resour. 22, 264–272 (in Chinese with English abstract).

Liang, X.R., Wei, G.J., Li, X.H., Liu, Y., 2003. Precise determination of $^{143}Nd/^{144}Nd$ and Sm/Nd ratios using multiple-collector inductively coupled plasmamass spectrometer (MC-ICPMS). Geochimica 32, 91–96 (in Chinese with English abstract).

Lin, Q., Ge, W., Sun, D., Wu, F., Won, C.K., Min, K.D., Jin, M.S., Wonlee, M., Kwon, C.S., Yun, S.H., 1998. Tectonic significance of Mesozoic volcanic rocks in northeastern China. Sci. Geol. Sin. 33, 129–139.

Lin, Q., Ge, W., Cao, L., Sun, D., Lim, K., 2003. Geochemistry of Mesozoic volcanic rocks in Da Hinggan Ling: the bimodal volcanic rocks. Geochimica 32, 208–222 (in Chinese with English abstract).

Lin, W., Faure, M., Monie, P., Scharer, U., Panis, D., 2008. Mesozoic extensional tectonics in eastern Asia: the south Liaodong Peninsula metamorphic core complex (NE China). J. Geol. 116, 134–154.

Liu, Y., Liu, H.C., Li, X.H., 1996. Simultaneous and precise determination of 40 trace elements in rock samples using ICP-MS. Geochimica 25, 552–558 (in Chinese with English abstract).

Liu, D., Zhao, Z., Zhu, D.C., Niu, Y., DePaolo, D.J., Harrison, T.M., Mo, X., Dong, G., Zhou, S., Sun, C., Zhang, Z., Liu, J., 2014. Postcollisional potassic and ultrapotassic rocks in southern Tibet: mantle and crustal origins in response to India–Asia collision and convergence. Geochim. Cosmochim. Acta 143, 207–231.

Ludwig, K.R., 2003. User's Manual for Isoplot 3.0: A Geolocronolgical Toolkit for Microsoft Excel, vol. 4. Geochronlogical Center Special Publication, pp. 1–70.

Luhr, J.F., Arandagomez, J.J., Housh, T.B., 1995. San-Quintin volcanic field, Baja–California–Norte, Mexico – geology, petrology, and geochemistry. J. Geophys. Res. – Solid Earth 100, 10353–10380.

Meng, Q.R., 2003. What drove late Mesozoic extension of the northern China-Mongolia tract? Tectonophysics 369, 155–174.

Menzies, M.A., Fan, W., Zhang, M., 1993. Palaeozoic and Cenozoic lithoprobes and the loss of >120 km of Archaean lithosphere, Sino–Korean craton, China, vol. 76. Geological Society, London, Special Publications, pp. 71–81.

Metelkin, D.V., Vernikovsky, V.A., Kazansky, A.Y., Wingate, M.T.D., 2010. Late Mesozoic tectonics of Central Asia based on paleomagnetic evidence. Gondwana Res. 18, 400–419.

Pearce, J., 1983. Role of the sub-continental lithosphere in magma genesis at active continental margins. In: Hawkesworth, c.J., Norry, M.J. (Eds.), Continental Basalts and Mantle Xenoliths, pp. 230–250.

Peccerillo, A., Taylor, S.R., 1976. Geochemistry of Eocene calc-alkaline volcanic rocks from the Kastamonu area, northern Turkey. Contrib. Miner. Petrol. 58, 63–81.

Pilet, S., Baker, M.B., Stolper, E.M., 2008. Metasomatized lithosphere and the origin of alkaline lavas. Science 320, 916–919.

Plank, T., Langmuir, C.H., 1998. The chemical composition of subducting sediment and its consequences for the crust and mantle. Chem. Geol. 145, 325–394.

Skora, S., Blundy, J., 2010. High-pressure hydrous phase relations of radiolarian clay and implications for the involvement of subducted sediment in arc magmatism. J. Petrol. 51, 2211–2243.

Sun, S.S., McDonough, W.F., 1989. Chemical and isotopic systematics of oceanic basalts: implications for mantle composition and process. In: Saunders, A.D., Norry, M.J. (Eds.), Magmatism in Oceanic Basins Geological Society London Special Publication, vol. 42, pp. 313–345.

Sun, H., Xiao, Y., Gao, Y., Lai, J., Hou, Z., Wang, Y., 2013a. Fluid and melt inclusions in the Mesozoic Fangcheng basalt from North China Craton: implications for magma evolution and fluid/melt–peridotite reaction. Contrib. Miner. Petrol. 165, 885–901.

Sun, D.Y., Gou, J., Wang, T.H., Ren, Y.S., Liu, Y.J., Guo, H.Y., Liu, X.M., Hu, Z.C., 2013b. Geochronological and geochemical constraints on the Erguna massif basement, NE China – subduction history of the Mongol–Okhotsk oceanic crust. Int. Geol. Rev. 55, 1801–1816.

Sun, W.D., Teng, F.Z., Niu, Y.L., Tatsumi, Y., Yang, X.Y., Ling, M.X., 2014. The subduction factory: geochemical perspectives. Geochim. Cosmochim. Acta 143, 1–7.

Syracuse, E.M., Abers, G.A., 2006. Global compilation of variations in slab depth beneath arc volcanoes and implications. Geochem. Geophys. Geosyst. 7.

Syracuse, E.M., van Keken, P.E., Abers, G.A., 2010. The global range of subduction zone thermal models. Phys. Earth Planet. Inter. 183, 73–90.

Tu, X.L., Zhang, H., Deng, W.F., Ling, M.X., Liang, H.Y., Liu, Y., Sun, W.D., 2011. Application of RESOlution in-situ laser ablation ICP-MS in trace element analyses. Geochimica 40, 83–98 (in Chinese with English abstract).

Turner, S., Hawkesworth, C., 1997. Constraints on flux rates and mantle dynamics beneath island arcs from Tonga-Kermadec lava geochemistry. Nature 389, 568–573.

Wang, F., Zhou, X.H., Zhang, L.C., Ying, J.F., Zhang, Y.T., Wu, F.Y., Zhu, R.X., 2006. Late mesozoic volcanism in the Great Xing'an range (NE China): timing and implications for the dynamic setting of NE Asia. Earth Planet. Sci. Lett. 251, 179–198.

Wang, F., Xu, W.L., Xu, Y.G., Gao, F.H., Ge, W.C., 2015. Late Triassic bimodal igneous rocks in eastern Heilongjiang Province, NE China: Implications for the initiation of subduction of the Paleo-Pacific Plate beneath Eurasia. J. Asian Earth Sci. 97, 406–423.

Wei, G.J., Liang, X.R., Li, X.H., Liu, Y., 2002. Precise measurement of Sr isotopic of liquid and solid base using (LP) MC-ICPMS. Geochimica 31, 295–299 (in Chinese with English abstract).

Wu, F.Y., Jahn, B.M., Wilde, S., Sun, D.Y., 2000. Phanerozoic crustal growth: U–Pb and Sr–Nd isotopic evidence from the granites in northeastern China. Tectonophysics 328, 89–113.

Wu, F.Y., Sun, D.Y., Li, H.M., Jahn, B.M., Wilde, S., 2002. A-type granites in northeastern China: age and geochemical constraints on their petrogenesis. Chem. Geol. 187, 143–173.

Wu, F.Y., Lin, J.Q., Wilde, S.A., Zhang, X.O., Yang, J.H., 2005. Nature and significance of the Early Cretaceous giant igneous event in eastern China. Earth Planet. Sci. Lett. 233, 103–119.

Wu, F.Y., Sun, D.Y., Ge, W.C., Zhang, Y.B., Grant, M.L., Wilde, S.A., Jahn, B.M., 2011. Geochronology of the Phanerozoic granitoids in northeastern China. J. Asian Earth Sci. 41, 1–30.

Xiao, W.J., Windley, B.F., Hao, J., Zhai, M.G., 2003. Accretion leading to collision and the Permian Solonker suture, Inner Mongolia, China: termination of the central Asian orogenic belt. Tectonics 22, 1069.

Yang, W., Li, S.G., 2008. Geochronology and geochemistry of the Mesozoic volcanic rocks in Western Liaoning: implications for lithospheric thinning of the North China Craton. Lithos 102, 88–117.

Yang, W.B., Niu, H.C., Shan, Q., Luo, Y., Sun, W.D., Li, C.Y., Li, N.B., Yu, X.Y., 2012. Late Paleozoic calc-alkaline to shoshonitic magmatism and its geodynamic implications, Yuximolegai area, western Tianshan, Xinjiang. Gondwana Res. 22, 325–340.

Yang, W.B., Niu, H.C., Sun, W.D., Shan, Q., Zheng, Y.F., Li, N.B., Li, C.Y., Arndt, N.T., Xu, X., Jiang, Y.H., Yu, X.Y., 2013. Isotopic evidence for continental ice sheet in mid-latitude region in the supergreenhouse Early Cretaceous. Sci. Rep. 3, 2732.

Yang, W.B., Niu, H.C., Shan, Q., Chen, H.Y., Hollings, P., Li, N.B., Yan, S., Zartman, R.E., 2014a. Geochemistry of primary-carbonate bearing K-rich igneous rocks in the Awulale Mountains, western Tianshan: implications for carbon-recycling in subduction zone. Geochim. Cosmochim. Acta 143, 143–164.

Yang, W.B., Niu, H.C., Shan, Q., Sun, W.D., Zhang, H., Li, N.B., Jiang, Y.H., Yu, X.Y., 2014b. Geochemistry of magmatic and hydrothermal zircon from the highly evolved Baerzhe alkaline granite: implications for Zr–REE–Nb mineralization. Miner. Deposita 49, 451–470.

Ying, J.F., Zhou, X.H., Zhang, L.C., Wang, F., 2010. Geochronological framework of Mesozoic volcanic rocks in the Great Xing'an Range, NE China, and their geodynamic implications. J. Asian Earth Sci. 39, 786–793.

Zhang, H.F., 2005. Transformation of lithospheric mantle through peridotite–melt reaction: a case of Sino-Korean craton. Earth Planet. Sci. Lett. 237, 768–780.

Zhang, J.H., 2009. Geochronology and Geochemistry of the Mesozoic Volcanic Rocks in the Great Xing'an Range, Northeastern China. Ph.D. Dissertation of China University of Geosciences, pp. 1–116 (in Chinese).

Zhang, H.F., Nakamura, E., Sun, M., Kobayashi, K., Zhang, J., Ying, J.F., Tang, Y.J., Niu, L.F., 2007. Transformation of subcontinental lithospheric mantle through peridotite–melt reaction: evidence from a highly fertile mantle xenolith from the north China Craton. Int. Geol. Rev. 49, 658–679.

Zhang, J.H., Ge, W.C., Wu, F.Y., Wilde, S.A., Yang, J.H., Liu, X.M., 2008a. Large-scale early cretaceous volcanic events in the northern Great Xing'an Range, northeastern China. Lithos 102, 138–157.

Zhang, L.C., Zhou, X.H., Ying, J.F., Wang, F., Guo, F., Wan, B., Chen, Z.G., 2008b. Geochemistry and Sr–Nd–Pb–Hf isotopes of Early Cretaceous basalts from the Great Xinggan Range, NE China: implications for their origin and mantle source characteristics. Chem. Geol. 256, 12–23.

Zhang, J.H., Gao, S., Ge, W.C., Wu, F.Y., Yang, J.H., Wilde, S.A., Li, M., 2010. Geochronology of the Mesozoic volcanic rocks in the Great Xing'an Range, northeastern China: implications for subduction-induced delamination. Chem. Geol. 276, 144–165.

Zhao, G.L., Yang, G.L., Fu, J.Y., 1989. Mesozoic Volcanic Rocks in the Central–Southern Da Hinggan Ling Range. Press of Science and Technology, Beijing (in Chinese).

Zhu, Y.F., Guo, X., Song, B., Zhang, L.F., Gu, L.B., 2009. Petrology, Sr–Nd–Hf isotopic geochemistry and zircon chronology of the Late Palaeozoic volcanic rocks in the southwestern Tianshan Mountains, Xinjiang, NW China. J. Geol. Soc. 166, 1085–1099.

Zorin, Y.A., 1999. Geodynamics of the western part of the Mongolia–Okhotsk collisional belt, Trans-Baikal region (Russia) and Mongolia. Tectonophysics 306, 33–56.